XV. PLASMAS AND CONTROLLED NUCLEAR FUSION

A. Active Plasma Systems*

Academic and Research Staff

Prof. L. D. Smullin   Prof. R. J. Briggs
Prof. A. Bers   Prof. J. G. Siambis

Graduate Students

R. R. Bartsch	B. R. Kusse	R. R. Parker
S. R. J. Brueck	R. K. Linford	D. M. Perozek
S-L. Chou	O. Lopez	H. M. Schneider
J. A. Davis	J. A. Mangano	R. E. Tremain, Jr.
F. N. Herba		R. N. Wallace

1. BEAM-PLASMA DISCHARGE: SYSTEM D

RF Oscillations Caused by a Low-Energy Beam

We have probed the afterglow of a beam-plasma discharge with a low-energy electron beam to study the interaction of the 100-500 V beam with a "hot-electron" plasma (electron temperature ~10-15 keV). The low-level beam is generated in the interpulse period with the circuits shown in Fig. XV-1. RF observations with a DC beam indicate that the low-level beam generates significant amounts of additional plasma. The additional plasma partially obscures the interaction of the low-level beam with the plasma from the main discharge. A pulsed beam is used to eliminate the
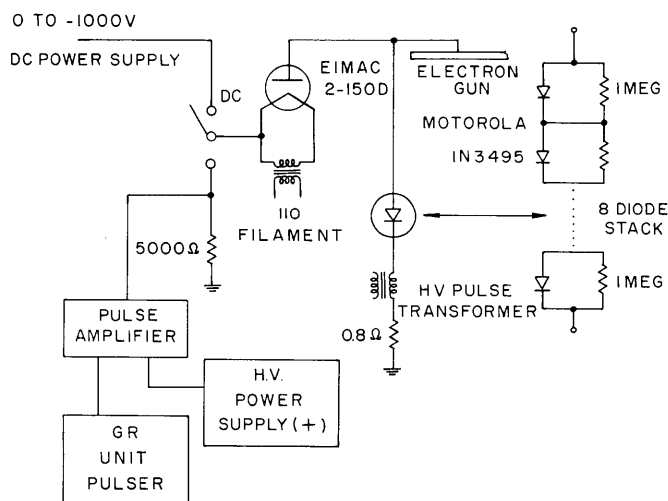

Fig. XV-1. Low-voltage-beam circuits.

plasma generated by the low-level beam. The pulse width is set to the maximum pulse width at which RF oscillations are not observed, because of the low-level beam by itself (~100 μsec). The repetition rate is typically set at 300/sec.

Oscillations are observed in the range 1-1000 Mc, with radio receivers (HP-8551B, SP-600A, BC-348N, Apr-4) and with resonant circuits and a wideband RF amplifier followed by a diode detector. A pickup loop at the wall of the discharge cavity was used for some of the DC beam observations. At present, the collector current is observed either across a resistance of ~0.1-1 Ω or with a parallel resonant circuit designed to
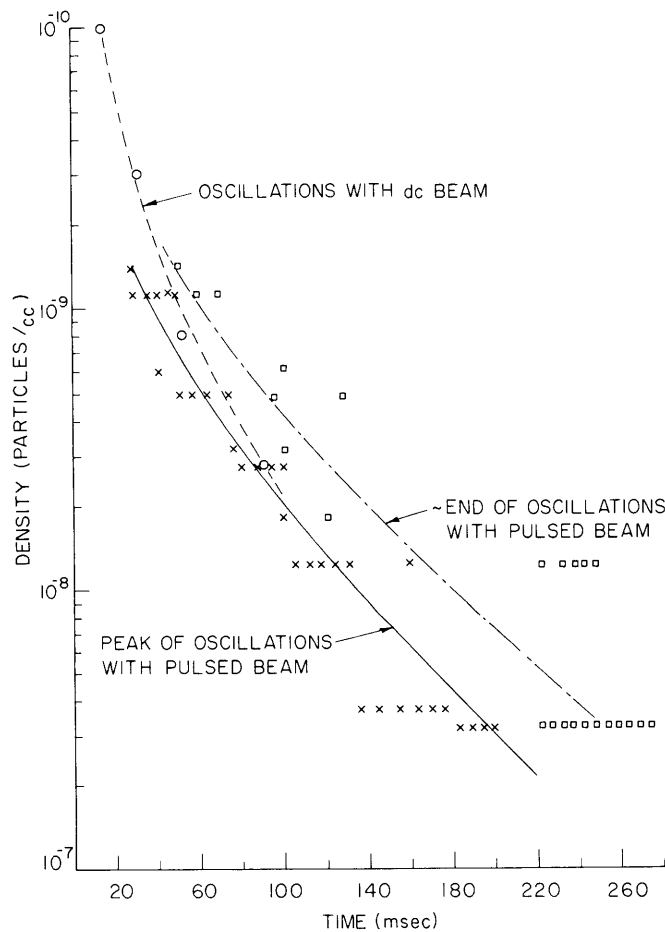

Fig. XV-2. Cold-electron density from beam-stimulated plasma frequency oscillations.

pass the main beam pulse (~700 μsec wide), and resonate at 1-10 Mc. High-frequency observations made with the APR-4 receiver for the DC beam and the HP-8551B for the pulsed beam are indicated in Fig. XV-2. The high-frequeny oscillations are interpreted

as electron plasma frequency oscillations at the plasma frequency of the cold electrons. The interaction of an electron beam with a hot-electron plasma has been discussed by Briggs for a one-dimensional system.[1] To apply Briggs' results to our observations, we must substitute ω_{pe}(cold) for ω_{pi} to account for the cold electrons. The condition for infinite amplification at $\omega = \omega_{pe\ cold}$ is given by

$$\frac{n_b}{n_p} \frac{T_e}{2V_o} > 1,$$

where n_b is the beam density, n_p is the <u>hot</u>-electron density, T_e is the temperature of the hot electrons (10-15 keV), and V_o is the beam voltage (500 V). The required condition on the hot-electron density is
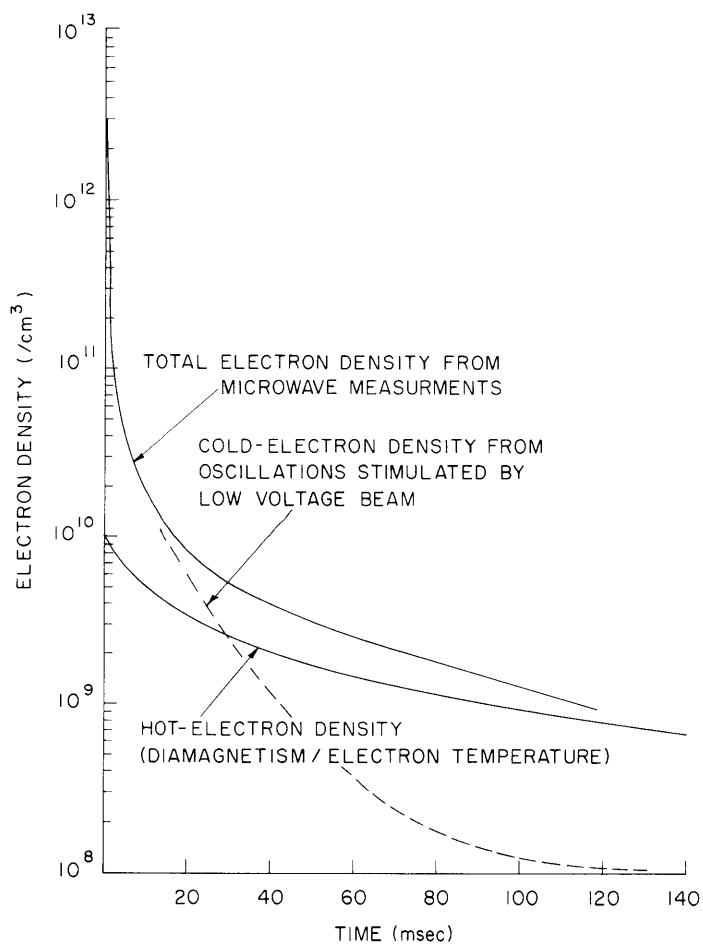

Fig. XV-3. Decay of electron density components.

$$n_p < n_b \frac{T_e}{2V_o} \sim 2 \times 10^9/cc.$$

This condition is met over the range of the observed oscillations for the pulsed beam at a beam voltage of 500 volts. The density decays for both the hot and cold components of the plasma are shown in Fig. XV-3. The methods used to measure the total density and the hot component are sufficiently inaccurate that only a qualitative check of the consistency of all three measurements is possible. We find that the ratio of hot-electron density to cold-electron density levels off at ~10.

Oscillations are observed in the range 1-10 Mc, coincident with the low-level beam pulses. The oscillations as detected across a parallel RLC collector ground connection are observed to start at 50-100 msec after the main discharge, peak at 100-150 msec, and die out after 200-300 msec. We shall study the details of the occurrence of the low-frequency oscillations with the rebuilt version of System D, and attempt to correlate the observations with the hot-electron-plasma, electron beam-ion interaction discussed by Briggs, Lieberman, Puri and Wallace.[1-4]

Electron Beam Density

The thickness of the electron beam has been determined from the slots cut by the (hollow) beam in support legs for the shorting plane placed in front of the gun (inside the beam) as shown in Fig. XV-4. The slot cut by the beam in the 3-mil thick tungsten vane
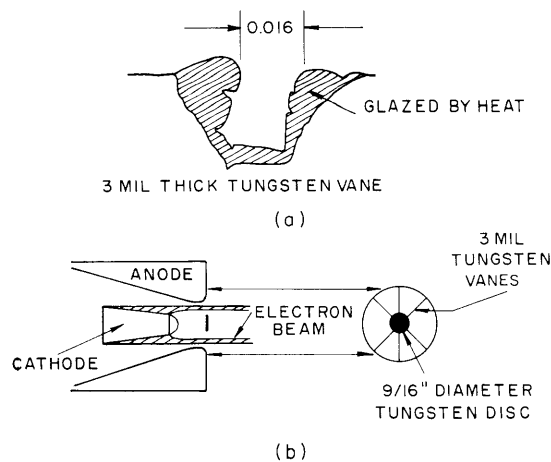

Fig. XV-4. (a) Slot cut by annular beam.
(b) Location of tungsten vanes.

is shown in Fig. XV-4a as determined by the optical comparator located in the R. L. E. machine shop. At the position of the gun the annular beam is found to be ~0.9 inch in diameter and 0.016 inch thick. For a 6-to-1 mirror ratio we find that the beam density in the center of the system is ~5 × 10^9/cc for a 15 kV beam and ~1.6 × 10^8/cc for

146

a 500-V beam, where the beam perveance has been assumed to be ~5.5 μperv.

The author wishes to acknowledge the use of the facilities of the National Magnet Laboratory for the experiments described here.

R. R. Bartsch

References

1. R. J. Briggs, Electron-Stream Interaction with Plasmas (The M.I.T. Press, Cambridge, Mass., 1964), Chap. 3.

2. M. A. Lieberman, Ph.D. Thesis, Department of Electrical Engineering, M.I.T., June 1966.

3. S. Puri, S.M. Thesis, Department of Electrical Engineering, M.I.T., June 1964.

4. R. N. Wallace, S.M. Thesis, Department of Electrical Engineering, M.I.T., September 1964.

2. SYSTEM C: EXCITATION OF AN ION-CYCLOTRON RESONANCE

Introduction

The discussion of a method of exciting an ion-cyclotron resonance by radiofrequency modulation of the electron beam normally used to generate a beam-plasma discharge is continued in this report.[1] As suggested by Smullin,[2] the modulation frequency has been chosen as the ion-cyclotron frequency, in order to excite a resonance in the azimuthal ion current. Such a resonance has been observed experimentally, and it has been associated with the excitation and propagation of the ion-cyclotron wave. In this report, experimentally obtained dispersion data are presented and compared with theory. From these data, information about some collisional damping processes in the plasma is obtained.

Experimental Apparatus

Figure XV-5 is a schematic diagram of the circuit used to modulate the DC electron beam, as well as a drawing of the discharge region. As shown in Fig. XV-5a, an RF pulse transformer is employed to modulate the DC beam pulse with 4 kV peak-to-peak of RF voltage. The driver and balanced output stages of an RF amplifier capable of 10 kW output is keyed to provide an RF pulse of variable width and starting time. Under normal operating conditions, a 350-μsec RF pulse is turned on 150 μsec after the start of the DC beam pulse. This DC pulse, which generates the beam-plasma discharge, has a width of 700 μsec and a repetition rate of 2 per second. An oscillogram of a typical beam-voltage pulse appearing at the cathode of the electron gun is shown in the lower left-hand corner of this figure. The modulation frequency may be varied from 1 to 4 mHz. For the experimental data to be reported here, the beam-plasma discharge was

(a)

(b)
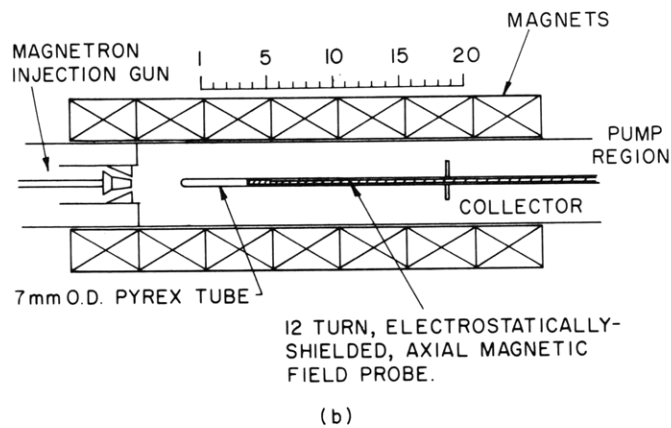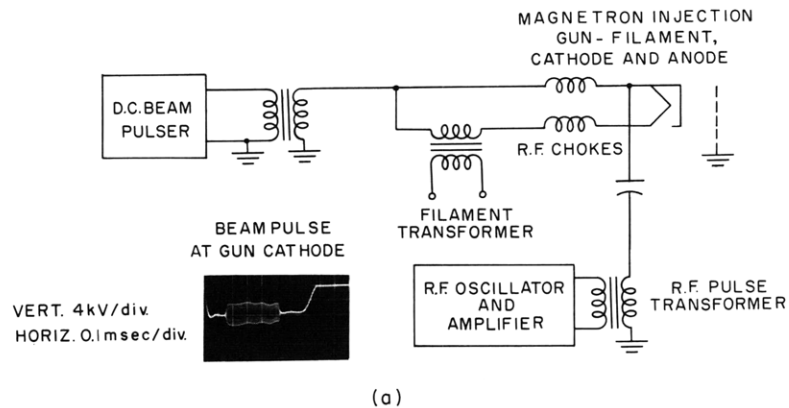
Fig. XV-5.　(a) Beam modulation circuit.
　　　　　　(b) Discharge region.

generated in hydrogen gas at an uncorrected Bayard-Alpert gauge pressure of 1.5×10^{-4} Torr. Figure XV-5b is a cross-section view of the discharge region which includes the magnets, magnetron injection gun, beam collector, and an RF axial magnetic field probe. The magnetron gun, whose driving circuit is shown in Fig. XV-5a, creates a hollow, high-perveance (10 µperv) electron beam. This electron beam, in turn, generates a cylindrical plasma column (approximately 6 cm in diameter) which is confined radially by the 7 magnet coils shown. The currents in these coils were chosen to provide a static magnetic field, B_o, which was constant along the entire length of the discharge region. An axially movable, electrostatically shielded RF magnetic field probe was inserted into the center of the plasma column to measure B_z, the axial component of the RF magnetic

field. The probe was isolated from the plasma by a Pyrex tube, 7 mm O. D., which was placed in the center of the hollow electron beam. This probe consists of 12 turns of Litz wire wound on a Teflon cylinder 3 mm in diameter. The output of the probe was filtered, and the magnitude and phase of the RF pulse were observed on an oscilloscope.

Experimental Observations

The first set of experimental data to be obtained is shown in Fig. XV-6. Here the amplitude of B_z is plotted against the driving frequency (the beam modulation frequency),
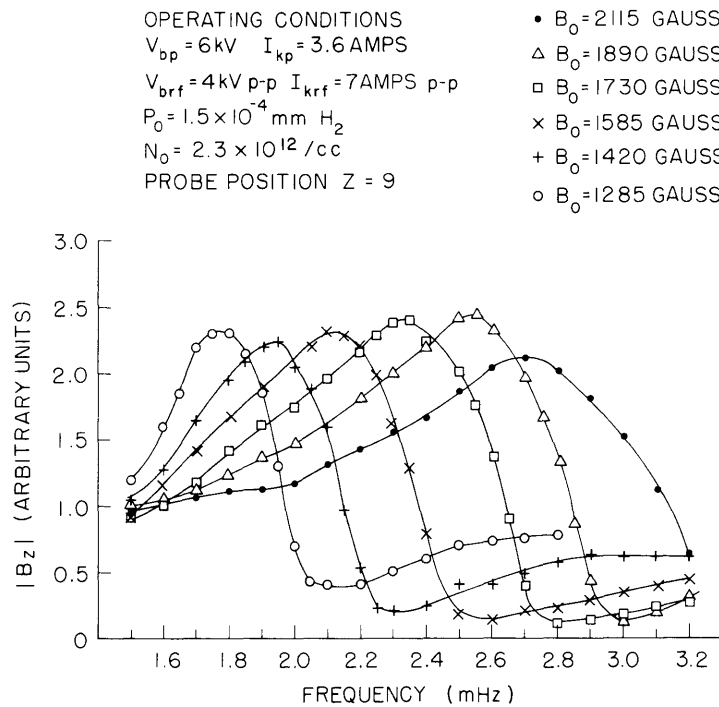

Fig. XV-6. Axial magnetic field as a function of frequency at a fixed probe position.

with the static magnetic field, B_0, as the varying parameter. In each case B_0 was constant along the entire length of the plasma column. All other beam-plasma variables were held constant at the values indicated. For these measurements the magnetic field probe was fixed at the axial position, z = 9. Qualitatively, these resonance curves show that the resonance frequencies increase nearly linearly with B_0.

Figure XV-7 is a plot of the measured static magnetic field, B_0, against the observed resonance frequencies. In each case the observed resonance frequency is below the predicted ion-cyclotron frequency. This apparent discrepancy may be explained

by postulating a wave, launched in the vicinity of the cathode, which propagates along the plasma column in the direction of increasing z. In order to determine the validity
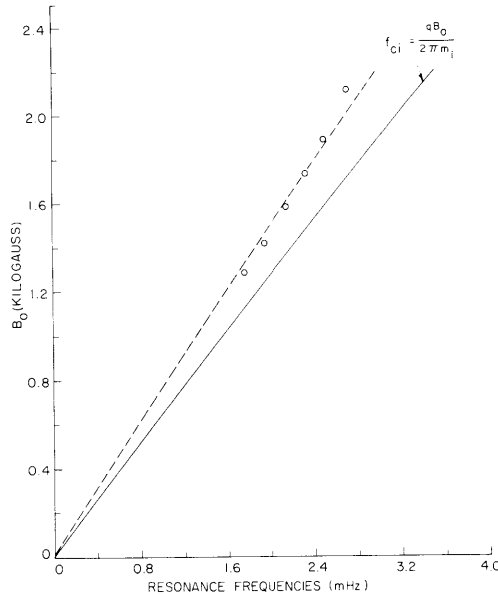

Fig. XV-7.

Measured static magnetic field, B_O, vs resonance frequencies.

of this hypothesis, the observed resonance was investigated experimentally for wave effects characteristic of the ion-cyclotron wave.

Magnitude and phase measurements of the axial RF magnetic field, B_z, were made as a function of the axial position, z, with the driving frequency, ω, as the varying parameter. Since the z dependence of B_z was assumed to be $e^{-j\beta(\omega)z}$, the real and imaginary parts of the axial wave number, $\beta = \beta_r + j\beta_i$, may be obtained from these data. When the phase data taken at each driving frequency were plotted against z in a linear coordinate system, essentially straight lines resulted. The slope of these lines was set equal to the real part of $\beta(\omega)$ at each frequency, since

$$\phi = \beta_r(\omega)z.$$

Similarly, the amplitude data were plotted against z on semilogarithmic paper. Again, at each driving frequency, essentially straight lines resulted whose linear slope was equal to the imaginary part of the axial wave number, β_i, at each frequency.

$$\log_e e^{-\beta_i z} = -\beta_i(\omega)z.$$

In both the magnitude and phase data, evidence of multiple mode excitation in the cathode region, and of a reflected wave near the collector was observed. These phenomena were detected as nonlinearities in the log magnitude and phase

plots near the cathode and collector.

Comparison of Theory and Experiment

It has been shown by Parker[4] that the theoretical dispersion relation of the ion-cyclotron wave propagating in a plasma column of radius $\underline{a}$ is given by

$$\beta^2 = k_o^2 K_\perp \left(1 - \frac{k_\perp^2}{k_o^2 K_{||}}\right),$$ (1)

where β is the axial wave number, $k_\perp \approx \frac{3.8}{a}$, $k_o = \frac{\omega}{c}$, and $K_\perp$ and $K_{||}$ are elements of the dielectric tensor given by

$$K_\perp = \frac{\omega_{pi}^2}{\omega_{ci}^2 - \omega^2 + j2\nu_i\omega}$$ (2)

$$K_{||} = \frac{\omega_{pe}^2}{j\omega(\nu_e + j\omega)}.$$ (3)

In these relations the effective ion collision-frequency ν_i is given by

$$\nu_i = \nu_{in} + \frac{7}{6}k_\perp^2 c_i^2 \frac{\nu_{ii}}{\nu_{ii}^2 + \omega_{ci}^2},$$ (4)

where ν_{in} is the ion-neutral collision frequency, and ν_{ii} is the ion-ion collision frequency as given, for example, in (3), and c_i is the ion thermal speed. A collision-dominated form of $K_{||}$ has been assumed in which ν_e is the effective electron-ion collision frequency. Other symbols appearing in (1), (2), and (3) have their usual meaning.

The theoretically and experimentally determined dispersion relations are compared in Fig. XV-8. The solid lines are the real and imaginary parts of β as determined from Eq. 1. In this plot the effective electron-ion collision frequency, ν_e, the effective ion collision frequency, ν_i, and the plasma density, n, were chosen to provide a best fit to the experimental data. The experimental dispersion data are represented by the plotted points in this figure. The value of plasma density for which best fit was obtained was n = 2.25 × 10^{12} particles/cc. Independent density measurements made with a 4-mm interferometer under the same operating conditions indicated an average electron density of 2.3 × 10^{12} particles/cc. Under the assumption of an effective plasma column radius of 3 cm, the value of ν_e which resulted in a best fit of theory to the experimental data was 2.42 × 10^7 collisions/sec. The value of ν_i which provided best fit was 470 × 10^3 collisions/sec.
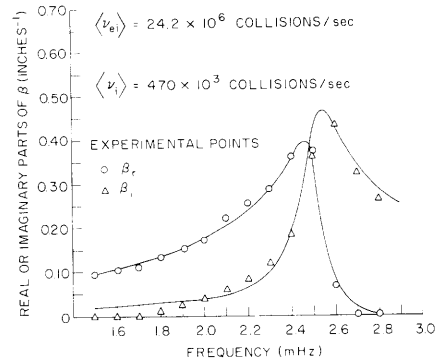
Fig. XV-8. Real and imaginary parts of the theoretical and experimental dispersion relations.

The theoretical value of ν_e found here may be compared with the theoretical value of the effective electron-ion collision frequency determined by Spitzer,[4] under the assumption of an average electron temperature of 4 electron volts. (Spectroscopic measurements[6] and Langmuir probe measurements[5] of electron temperature have indicated an average electron temperature of 4 eV.) This formula predicts a value of ν_e equal to approximately 0.2 times the experimental value. The experimental value of ν_e, however, depends strongly on the effective plasma column radius assumed in Eq. 1. Since the plasma column is radially inhomogeneous (Eqs. 1-4 were derived under the assumption of a homogeneous plasma column), the actual value of the radial wave number $k_\perp$ that should be used here is not known. For example, if an effective plasma column radius of 1 cm is used, good agreement between theory and experiment is obtained. Another possible explanation for the anomalously large experimental value of ν_e is Landau damping of the wave by plasma electrons which move along the static magnetic field lines to neutralize the polarization charge of the ions. This collisionless damping would manifest itself in $K_\parallel$ as an increase in the effective electron-ion collision frequency. The effects of Landau damping on ion-cyclotron waves have been investigated,[5] and it has been shown that under certain conditions the Landau damping can be very strong. More experimental data are required in order to assess the relevance of this effect.

Equation 4 may be used to obtain a "theoretical" value of ν_i. The effective ion-neutral collision frequency, ν_{in}, was determined from an extrapolation of experimentally obtained cross sections.[7] Calculations based on these data, under the assumption of a corrected Bayard-Alpert gauge pressure of 0.7 micron, result in a value for ν_{in} of 213×10^3 collisions/sec. The actual neutral-gas pressure, however, may be as much as twice this. (A more accurate pressure measurement is, at present, being performed.) If this were true, ion-neutral collisions would account for essentially all of the measured effective ion collision frequency. The contribution to ν_i, resulting from the effective

collision frequency caused by ion-ion collisions is given by

$$(\nu_i)_{ii} = \frac{7}{6} k_\perp^2 c_i^2 \frac{\nu_{ii}}{\nu_{ii}^2 + \omega_{ci}^2}.$$

For an ion temperature of 1 eV and a plasma column radius of 3 cm, this term is approximately two orders of magnitude below the observed effective ion collision frequency. Corrections to this term through $K_\perp$, arising from the radial inhomogeneity of the plasma column, will increase its contribution, however. Observations of the resonance curve with changes in neutral-gas pressure and density indicate, however, that the dominant term in ν_i is due to ion-neutral collisions.

The resonant curves shown in Fig. XV-6, which were measured at a probe position of z = 9, were extrapolated to the point of excitation of the wave at z = -2. This extrapolation was accomplished by using the theoretical imaginary parts of the axial wave number β. The corrected resonance frequencies are plotted against the measured
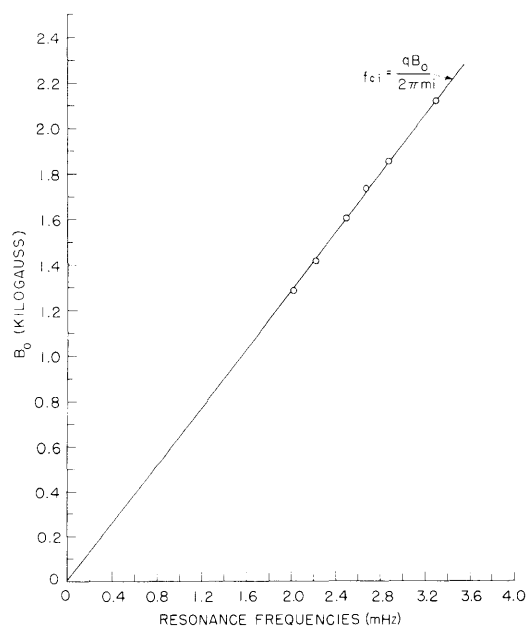

Fig. XV-9.
Measured static magnetic field, B_o,
vs corrected resonance frequencies.

static magnetic field, B_o, in Fig. XV-9. Close agreement between the observed resonance frequencies and the ion-cyclotron frequencies is now found.

Summary

The experimental and theoretical dispersion relations for the ion-cyclotron wave propagating in a partially filled waveguide have been compared. As shown in Fig. XV-8,

the real and imaginary parts of the axial wave number β, could be made to agree quite closely with the theoretically obtained β, by adjusting the density and the effective ion and electron-ion collision frequencies. The value of the average plasma density agrees quite well with 4-mm interferometer density measurements. The experimental value of the effective electron-ion frequency, however, is greater than the corresponding theoretical value. One probable cause of this discrepancy is an uncertainty in the value of $k_\perp$ which is used to obtain the experimental value of v_e. This uncertainty is due to the radial inhomogeneity of the plasma column, and could be resolved by a theoretical investigation of the inhomogeneous plasma column. The experimentally obtained value of v_i was also greater than the predicted value. The major part of this discrepancy may be associated with an uncertainty in the neutral-gas pressure in the system. Also, a larger contribution from ion-ion collisions may be expected when the radial inhomogeneity of the plasma column is considered.

J. A. Mangano, R. R. Parker

References

1. J. A. Mangano, "System C: Excitation of an Ion-Cyclotron Resonance," Quarterly Progress Report No. 85, Research Laboratory of Electronics, M. I. T., April 15, 1967, pp. 141-145.

2. L. D. Smullin, "Beam-Plasma Discharge: Excitation of Ions at the Ion-Cyclotron Frequency (Theory)," Quarterly Progress Report No. 80, Research Laboratory of Electronics, M. I. T., January 15, 1966, pp. 111-113.

3. I. P. Shkarofsky, I. B. Bernstein, and B. B. Robinson, "Condensed Presentation of Transport Coefficients in a Fully Ionized Plasma," Phys. Fluids 6, 40-47 (1963).

4. L. Spitzer, Jr., Physics of Fully Ionized Gases (Interscience Publishers, New York, revised edition, 1962).

5. R. R. Parker, "Excitation and Propagation of Ion-Cyclotron Waves in a Plasma Column," Sc. D. Thesis, Department of Electrical Engineering, M. I. T., 1967.

6. R. D. Reilly, "Linear Systems Approach to a Problem in Plasma Spectroscopy," S. M. Thesis, Department of Electrical Engineering, M. I. T., 1966.

7. J. H. Simons, C. M. Fontana, E. E. Muschlitz, Jr., and S. R. Jackson, "The Low Velocity Scattering of H^+ and H_3^+ in Hydrogen," J. Chem Phys. 11, 307-312 (1943).

3. INTERACTION OF A SPIRALING ELECTRON BEAM WITH A PLASMA

An interesting, low-pressure, beam-plasma discharge has been observed by using our spiraling electron beam.[1] This interaction appears to occur only when the electron beam possesses DC kinetic energy across the magnetic field. Two types of beams have been used to study this effect: a hollow cylindrical, straight-flowing beam, and a hollow, cylindrical, spiraling beam.

The electron beams are approximately 2 inches in diameter and 0.12 inch thick. The

ends of the interaction region are defined by the anode and collector. This region is surrounded by a stainless-steel screen, 4 inches in diameter (see Fig. XV-10). An
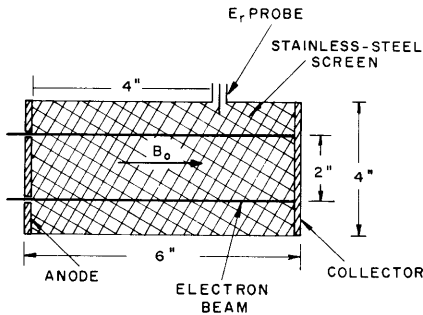

Fig. XV-10.   Beam-plasma interaction region.

axial magnetic field, uniform within 3 per cent exists inside the screen.

By operating with argon gas at a background pressure of 3.8×10^{-5} mm Hg and using a straight-flowing beam, ionization occurred only in the region of the electron beam. Beam voltages from 0 to 600 volts and perveances from 0 to approximately 30 μperv were used, but the plasma emitted light only in the region of the beam electrons.
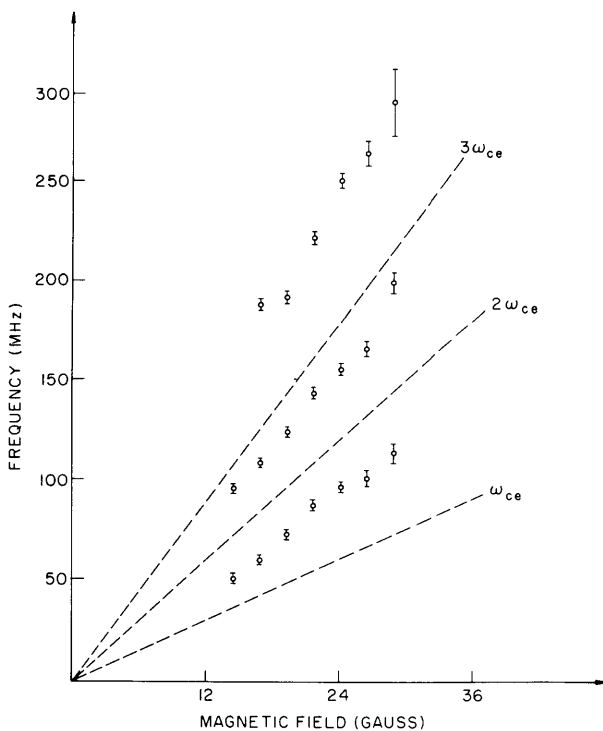

Fig. XV-11.   Observed frequency vs mag-
netic field.

By using a spiraling electron beam with argon gas at 3.8×10^{-5} mm Hg, however, it was possible to produce a discharge and observe light coming from the entire region inside the stainless-steel screen. The discharge was established as follows: A spiraling electron beam was formed[1] with approximately 1/3 of its total DC kinetic energy in azimuthal motion. Under these conditions, no discharge was observed, only ionization in the path of the beam. The axial beam energy was then decreased and the azimuthal energy was kept constant. When the axial and azimuthal energies were approximately equal, the discharge set in. Reducing the axial beam energy further resulted in a brighter discharge.

During this spiraling beam-plasma discharge, the voltage on the radial

electric field probe (see Fig. XV-10) was observed on a spectrum analyzer. Signals were found at frequencies slightly above the electron-cyclotron frequency and its first and second harmonics. These frequencies, which were not present on the straight-flowing beam, were observed as the axial magnetic field was varied, and the results are shown in Fig. XV-11. The points indicate the peak of the observed spectrum, and the brackets are used to show the frequency spread. The signals above ω_{ce} and $3\omega_{ce}$ were approximately 20 dB stronger than those above $2\omega_{ce}$. The azimuthal beam velocity is proportional to the square of the magnetic field strength. In all cases shown in Fig. XV-11 the axial beam energy was adjusted to give the largest observed signal.

Two general observations can be made from these data. First, the spectrum width increases as the magnetic field increases. Second, if the oscillations are compared with the closest cyclotron harmonic below them in frequency, the difference between their frequency and the harmonic increases with increasing magnetic field.

We intend to continue the study of these oscillations to determine their role in the rotating beam-plasma discharge.

B. Kusse, A. Bers

References

1. B. Kusse and A. Bers, "Cross-Field Beam-Plasma Interaction," Quarterly Progress Report No. 82, Research Laboratory of Electronics, M.I.T., July 15, 1966, pp. 154-157.

4. COMPUTER SIMULATION OF THE BEAM-PLASMA INTERACTION

We have introduced charge disks to represent the beam, while the plasma is assumed to be infinite, cold, lossless, and linear. There is no magnetic field, but the beam is not allowed to have any transverse motion.[1] The fields generated by a disk moving through a plasma have been found,[2,3] for a uniform plasma and a constant-velocity disk. There are two fields, a wake field and a nonoscillatory field. The acceleration on another disk, owing to the wake field, is

$$a(z,t) = \frac{-Q^2}{M\epsilon_0}[1 - 2I_1(a)K_1(a)]\cos\left[\omega_p\left(t - \frac{z}{v_0}\right)\right]u_{-1}\left(t - \frac{z}{v_0}\right), \tag{1}$$

where M is the disk surface mass density (Kg/m^2), Q is the disk surface charge density, $a = \omega_p b/v_0$, b is the beam radius, I_1 and K_1 are the modified Bessel functions of second kind, and u_{-1} is the unit step function. In this case, $a = 3.18$, corresponding to parameters in System A. The acceleration on another disk because of the nonoscillatory field ahead of the disk is
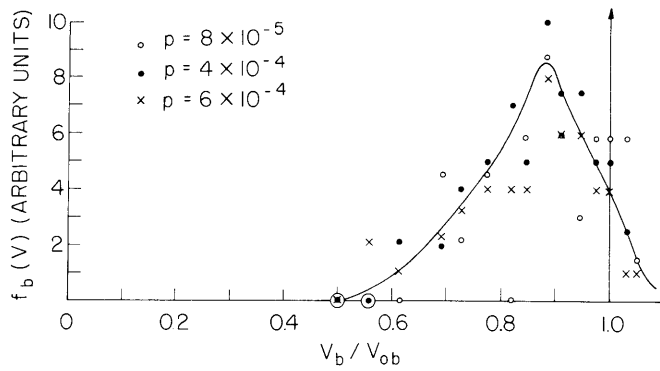
Fig. XV-12. Snapshot of beam disk velocity vs distance, and a snapshot of test disk acceleration vs distance, with plasma density gradient. Distances are normalized to $0.2 v_o/\omega_{po}$.
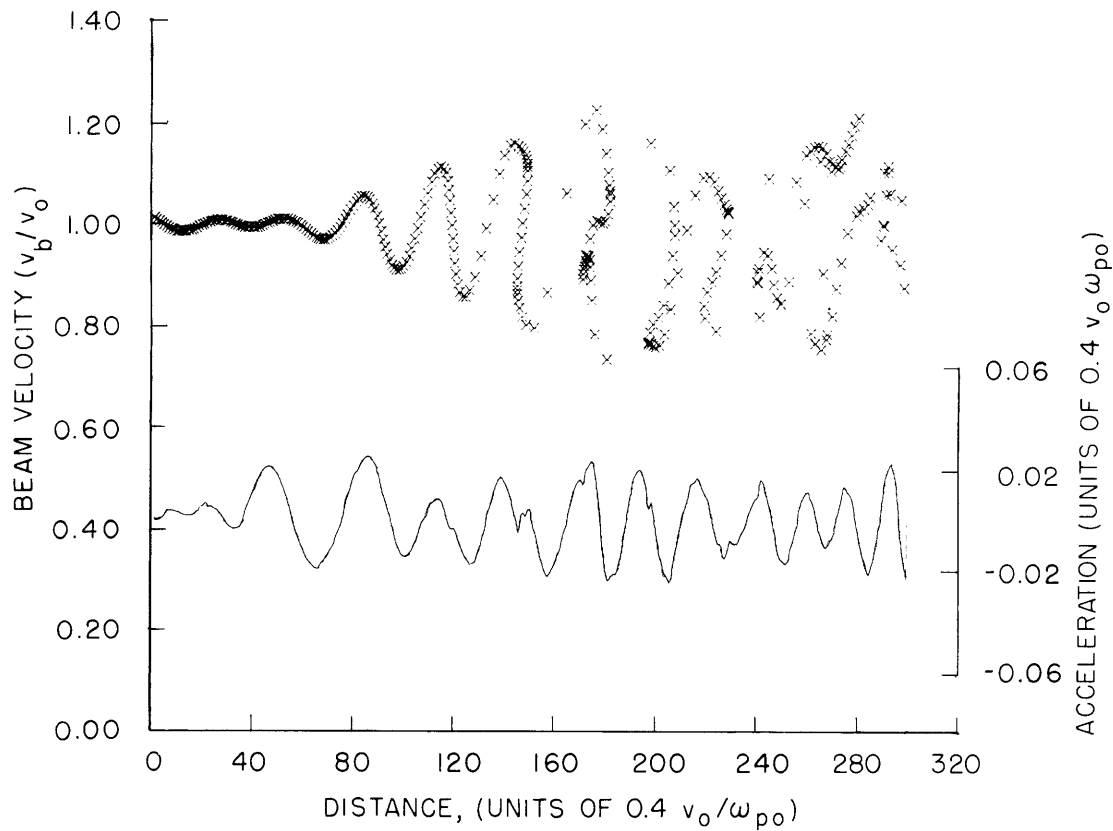

Fig. XV-13. Collected beam velocity distribution.

$$a(z,t) = \frac{Q^2}{M\epsilon_0} \int_0^\infty \frac{dx\ xJ_1^2(x)\ \exp[-x\Delta z/b]}{x^2 + a^2},$$

(2)

where Δz is the disk separation. The nonoscillatory field behind the disk is the mirror image of the field ahead.

We want to allow for variations in $\omega_p(z)$ and disk velocity. We do this approximately as follows. To calculate the wake field at a plane z, we use Eq. 1, with the local $\omega_p(z)$ and the velocity that the disk has when it passes z. To calculate the nonoscillatory field at a plane z, we use the local $\omega_p(z)$ and the present velocity of the disk. The computer results are shown in Fig. XV-12. The beam is velocity-modulated at z = 0 over a frequency band extending from $(0.15)^{1/2}\ \omega_{po}$ to 0.5 ω_{po}. This simulates the effects of plasma fluctuations of energy density nκT. The plasma frequency in this case varies spatially as

$$\omega_p^2(z) = \omega_{po}^2 \sin(0.15 + az).$$

(3)

The first-order plasma parameters remain small $(v_p/v_0 \approx \rho_p/\rho_{op} \approx 0.03)$, thereby justifying our assumption of plasma linearity.

The interaction length shown is approximately 20 per cent of that in System A. The beam velocity spread shown in Fig. XV-12 is comparable to the collected beam velocity spread found in System A, in contrast to previous results with one-dimensional beams in a uniform plasma,[5] and with plasma density gradients.[6] The measured beam velocity distribution in System A is shown in Fig. XV-13.

J. A. Davis

References

1. J. A. Davis, Quarterly Progress Report No. 85, Research Laboratory of Electronics, M. I. T., April 15, 1967, pp. 178-182.

2. R. W. Gould and M. A. Allen, 5e Congrès International. Tubes pour Hyperfréquences, p. 445 (1964).

3. R. W. Gould, "High Power Beam-Plasma Amplifier," Report No. 2, Microwave Associates, 1963, p. 8.

4. In this calculation we let the region 0 < z < 200 approach a steady state, collecting sheets at z = 200, before letting sheets excite fields beyond z = 200. Then we allowed sheets to reach z = 250 before collecting. After a steady state was approached again, sheets were allowed to reach z = 300. This was done to avoid the large transient fields that would be excited downstream by initial beam overtaking, which occurs far downstream early in the transient build-up.

5. J. A. Davis, Quarterly Progress Report No. 82, Research Laboratory of Electronics, M. I. T., July 15, 1966, pp. 146-151.

6. J. A. Davis, Quarterly Progress Report No. 84, Research Laboratory of Electronics, M. I. T., January 15, 1967, pp. 145-148.

5. DYNAMICS OF THE PLASMA BOUNDARY

We have previously investigated the dynamics of electrons that follow a uniform dis-placement perturbation for a plasma slab with sharp boundaries.[1,2] In this report we present some of the new aspects of this work for the case in which the plasma slab has a finite density gradient.

Results of Computer Experiments

Assume that the plasma slab of thickness d is cold and in equilibrium, and has elec-trons and ions distributed with equal density n(x) over a thickness d, as shown in Fig. XV-14. Both the ion and electron charge distributions are modeled by a discrete
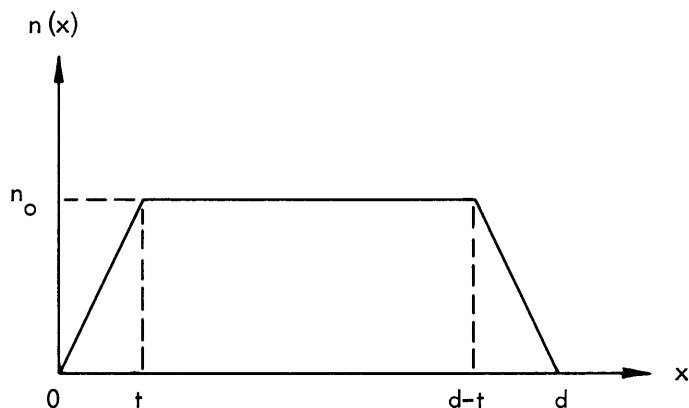
Fig. XV-14. Plasma slab.

number of charge sheets, with the same charge per unit area on each sheet. The non-uniformity in the tapered regions (0 < x < t and (d-t) < x < d) is modeled by a variable sheet spacing. The ions are treated as immobile, and the trajectories of the electron sheets are computed after all the sheets have been given a uniform displacement δ in the x-direction. The electron sheet trajectories are given in Fig. XV-15 for t/d = 0.25 and δ/d = 0.04. The first crossing of electron trajectories occurs in less than one plasma period of the central electrons. The new aspect of these results is that the crossing particles were not originally displaced outside the ion background, as was the case for a slab with sharp boundaries.[3] Figure XV-16 shows electron sheet trajectories when t/d = 0.25 and δ/d = 0.12, which is a larger perturbation than that given in Fig. XV-15. In this case, the first crossing occurs in less than half a plasma period of the central electrons. This crossing time is shorter than that for the sharply bounded case. Note also that the first crossing takes place near the bottom of the slab for this initial displacement.
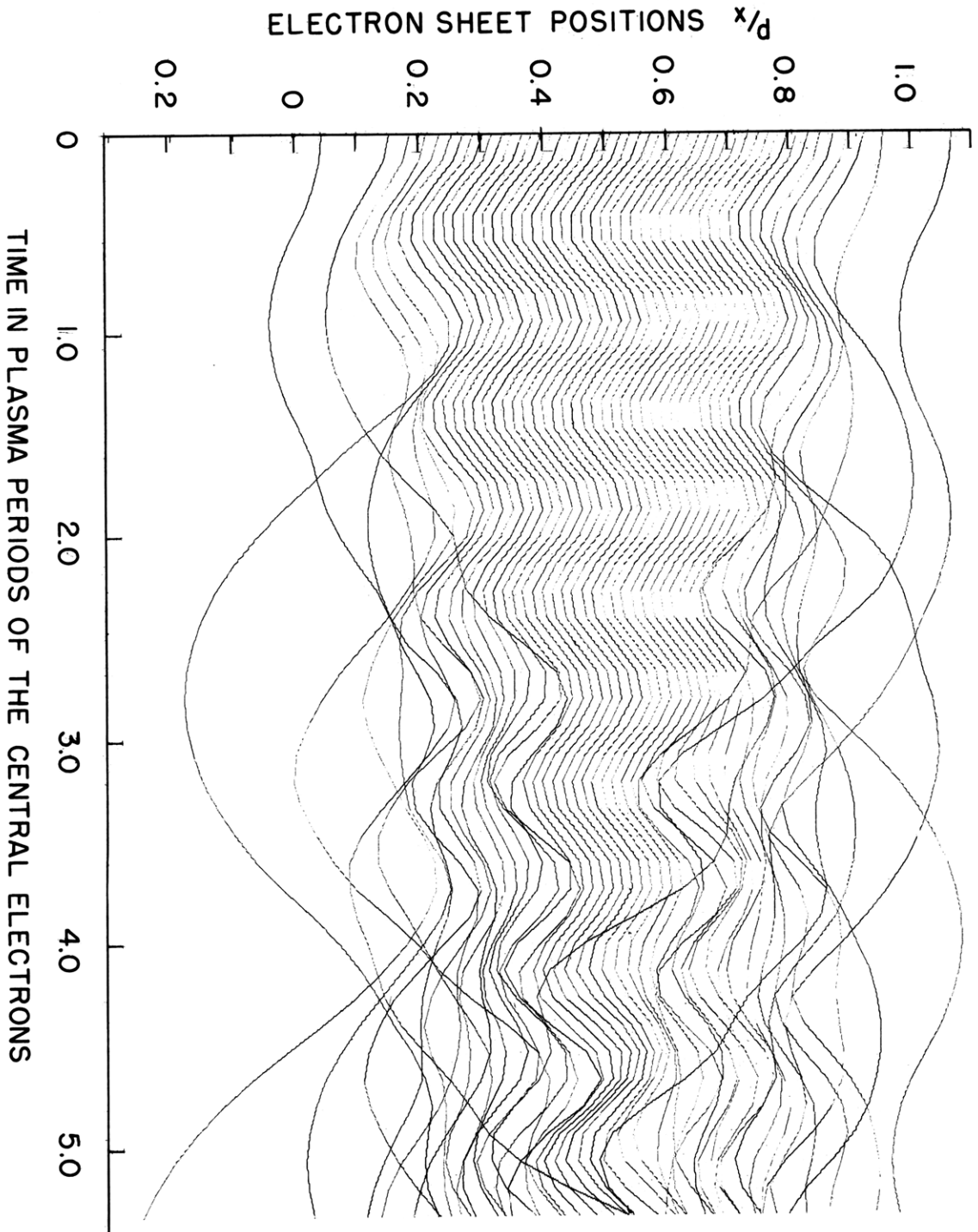
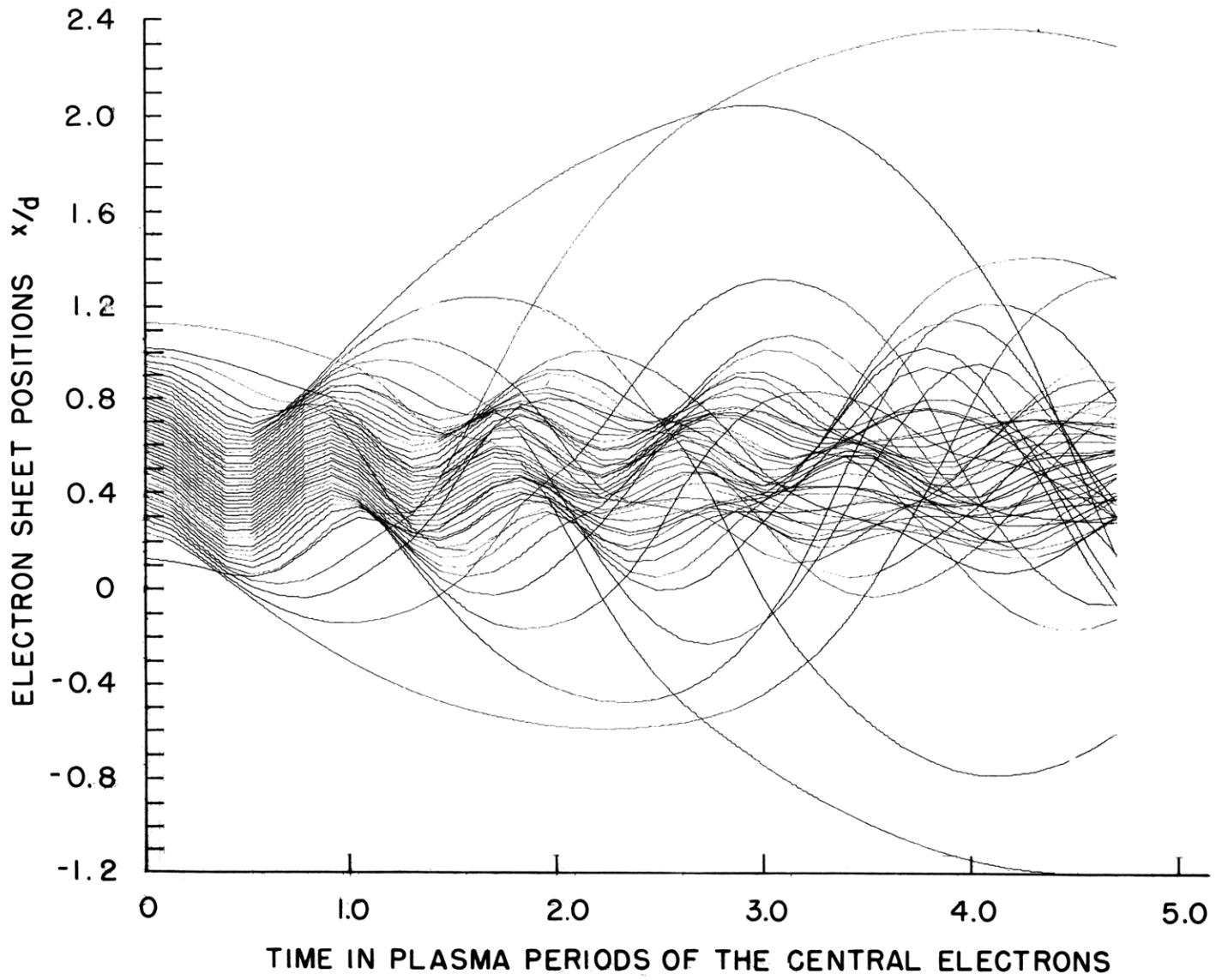Fig. XV-15. Time in plasma periods of the central electrons.

Fig. XV-16. Time in plasma periods of the central electrons.

In the sharply bounded slab, the time of first overtaking is independent of the amplitude of the displacement perturbation, and the crossing always takes place near the top of the slab.[3] In the slab with tapered boundaries, the time of first crossing and the location in the slab depends on the amplitude of the initial displacement.

Crossing Time for Oscillations in a Nonuniform Slab

Consider a cold plasma slab of thickness d which has an equilibrium density distribution for ions and electrons, $n(x)$. If the ions are assumed to have infinite mass, the equation of motion for an electron having instantaneous position x and unperturbed position x_o is[3]

$$m \frac{d^2 x}{dt^2} = - \frac{e^2}{\epsilon_o} \int_{x_o}^{x} n(x') \, dx',$$ (1)

as long as the electron remains inside the slab. If the displacement from equilibrium is small, Eq. 1 may be linearized as follows:

$$\frac{d^2 x}{dt^2} = -\omega_p^2(x_o)(x-x_o),$$ (2)

where $\omega_p(x_o)$ is the local plasma frequency. For an initial displacement perturbation, the conditions are $x = x_o + \delta$ and $dx/dt = 0$ at $t = 0$. The solution of Eq. 2 is

$$x = x_o + \delta \cos \omega_p(x_o)t.$$ (3)

Applying the overtaking condition $\partial x/\partial x_o = 0$ to Eq. 3 gives

$$\omega_p t_o \sin \omega_p t_o = \frac{\omega_p}{\delta \omega_p'},$$ (4)

where $\omega_p' = d\omega_p/dx_o$, and t_o is the overtaking time. The earliest overtaking occurs when $\partial t_o/\partial x_o = 0$, or

$$[\omega_p t_o]^2 \cos \omega_p t_o = - \frac{\omega_p'' \omega_p^2}{\delta(\omega_p')^3}.$$ (5)

In Fig. XV-17 we show a graphical solution to Eq. 4 when x_o and δ are known. We have assumed that $\omega_p(x_o)$ is symmetric about the center of the slab, so that there are two places where $|\omega_p'(x_o)|$ = constant; only their signs will be different. For large initial displacements, a crossing will first occur where ω_p' is positive ($x_o < d/2$). As the displacement δ decreases, a crossing occurs first for $x_o > d/2$. This explains the change in location of the first crossings as a function of initial amplitude indicated in

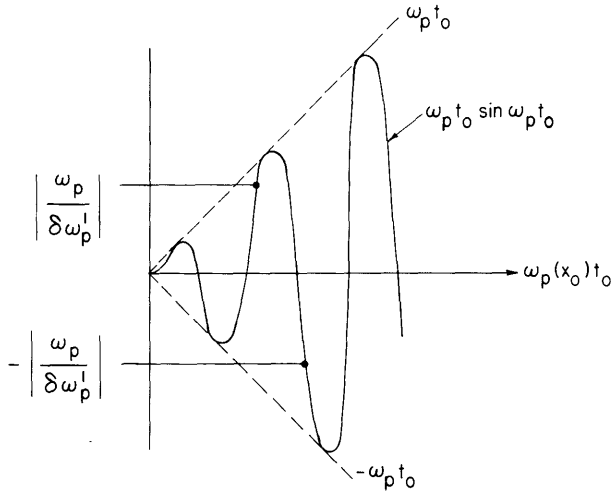Fig. XV-17. Graphical solution to Eq. 4.

the computer experiments given in Figs. XV-15 and XV-16.

If the initial displacement is very small, an approximate solution to Eq. 4 is

$$t_o \approx \frac{1}{\delta \omega_p'}. \tag{6}$$

The first crossing occurs where $\omega_p'' = 0$, or where ω_p' is a maximum, and the time of crossing is inversely proportional to the initial displacement.

The result in Eq. 6 agrees, except for a numerical factor, with that obtained by Dawson.[4] His analysis is an approximate one and predicts crossings at times that are always greater than those given in Eq. 6.

Numerical Example

Equation 1 has been solved for the smooth density distribution

$$n(x) = \frac{n_o}{4} \left(1 - \cos \frac{2\pi x}{d}\right)^2 \qquad 0 < x < d. \tag{7}$$

The plasma frequency is, therefore,

$$\omega_p(x_o) = \omega_{po} \frac{1}{2} \left(1 - \cos \frac{2\pi x_o}{d}\right) \qquad 0 < x_o < d, \tag{8}$$

and is given in Fig. XV-18. Note that ω_{po} is the plasma frequency in the center of the slab. The equation of motion for the electrons inside the slab becomes

$$\omega_p(x_o) = \frac{\omega_{po}}{2} \left(1 - \cos \frac{2\pi x_o}{d}\right)$$

Fig. XV-18. Plasma frequency.

$$\frac{d^2x}{dt^2} = -\frac{1}{4}\omega_{po}^2\left[\frac{3}{2}(x-x_o) + \frac{d}{\pi}\left(\sin\frac{2\pi x_o}{d} - \sin\frac{2\pi x}{d}\right) + \frac{d}{8\pi}\left(\sin\frac{4\pi x}{d} - \sin\frac{4\pi x_o}{d}\right)\right] \quad (9)$$

Equation 9 has been integrated numerically. The results are given in Fig. XV-19 for an initial displacement perturbation $\delta/d = 0.1$. The lines in Fig. XV-19 are the integrated
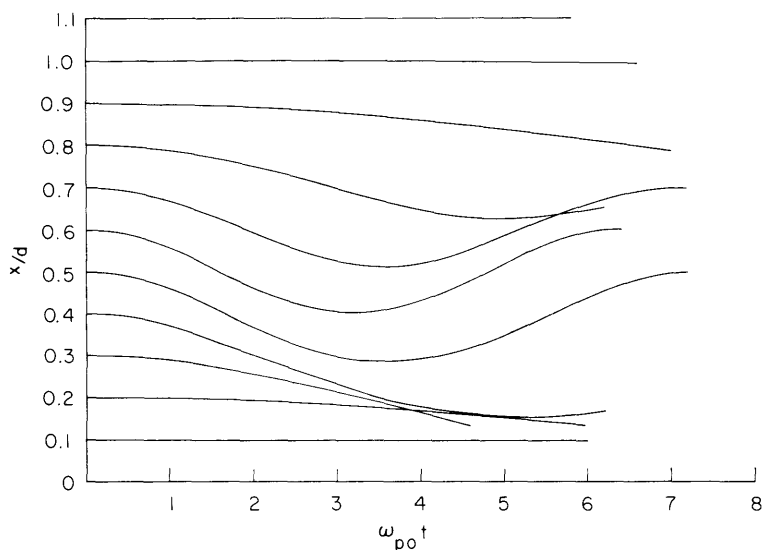

Fig. XV-19. Results of integration of Eq. 9.

trajectories $x(x_o, t)$ for values of x_o/d between 0.0 and 1.0 in steps of 0.1. The first crossing occurs at the bottom of the slab for x_o/d between 0.1 and 0.2, whereas the linearized theory for small displacements would predict crossing where $\omega_p'' = 0$; for the density distribution given by Eq. 8 this occurs at $x_o/d = 0.25$ or $x_o/d = 0.75$.

H. M. Schneider

References

1. H. M. Schneider, Phys. Fluids 9, 2299 (1966).

2. H. M. Schneider, Quarterly Progress Report No. 84, Research Laboratory of Electronics, M. I. T., January 15, 1967, p. 149.

3. W. M. Leavens and I. B. Leavens, Radio Sci. 1, 789 (1966).

4. J. M. Dawson, Phys. Rev. 113, 383 (1959).

6. CYCLOTRON RESONANCE OF CHARGED PARTICLES IN THE PRESENCE OF NONUNIFORM ELECTRIC FIELD AND STATIC MAGNETIC FIELD

The work reported in Quarterly Progress Report No. 85 (pages 186-192) has been extended. Particles whose guiding center is initially located at approximately 0.2 of the maximum radial distance have been studied with the same parameters used as in the previous report. The numerical results for the exact fields of interest are compared with: (a) the case of uniform static magnetic field and uniform electric field at resonance, $\omega = \omega_B$; and (b) the case of uniform static magnetic fields and uniform electric field off-resonance, $\omega \neq \omega_B$.

The trajectories that were studied can be classified as follows: Class I, particles that stay in the midplane; Class II, particles that stay close to the midplane; and Class III, particles that move far away from the midplane (see Appendix A).

Results

Trajectories of Class I

a. See Fig. XV-20 (also Appendix A). The initial velocity is in phase with the electric field. The energy, magnetic moment, and radial position of the guiding center
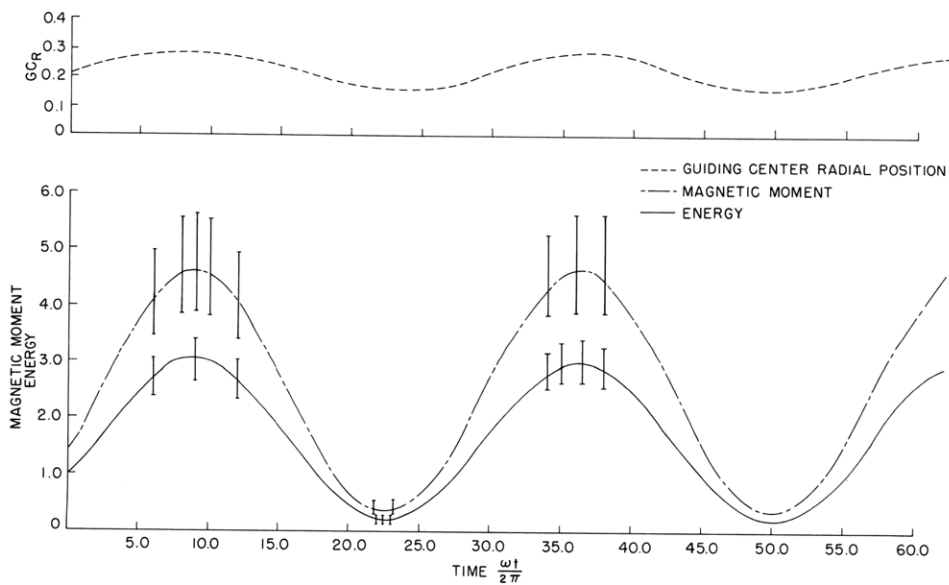

Fig. XV-20. Energy, magnetic moment, and radial position of the guiding center as a function of time for a particle in the midplane starting in phase with the electric field.

exhibit periodic behavior with a period equal to 27 periods of the applied electric field. The trajectory has been followed up to 183 periods of the applied electric field and no

significant change has been observed in the pattern of behavior. The guiding center drifts clockwise, completing one revolution around the mirror axis in ~19 periods of the applied electric field. The time behavior of the energy is similar to the uniform static magnetic field and off-resonance electric field case, having a $\Delta\omega = \omega - \omega_B \approx 0.55$. The energy gain predicted from the uniform fields case has a value of ~0.15, while we observe energy gains one order of magnitude higher. The particle samples a large range of values of the magnetic field. (At the points where the energy is maximum, the Larmor radius is ~0.25, and the value of the magnetic field (B) is ~0.735, while at an energy minimum the Larmor radius is ~0.06, B ~ 0.797; B resonance = 0.76.)

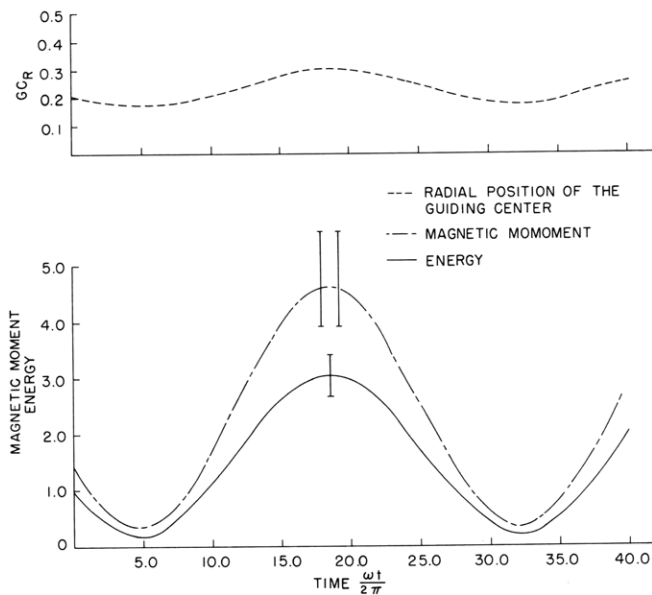   b. See Fig. XV-21. The initial velocity is out of phase with the electric field. The

Fig. XV-21. Energy, magnetic moment, and radial position of the guiding center as a function of time for a particle in the midplane starting out of phase with the electric field.

energy, magnetic moment, and radial position of the guiding center exhibit periodic behavior with the same period as in the previous case. The behavior is very similar, except for the fact that the energy, magnetic moment, and radial position of the guiding center decrease initially.

Trajectories of Class II

    a. See Figs. XV-22 and XV-23. The initial velocity is in phase with the electric field. The energy, magnetic moment and radial position of the guiding center behave in

a fashion similar to the corresponding case for trajectories of Class I, but the maxima of the energy and magnetic moment increase slightly (during the time that we have
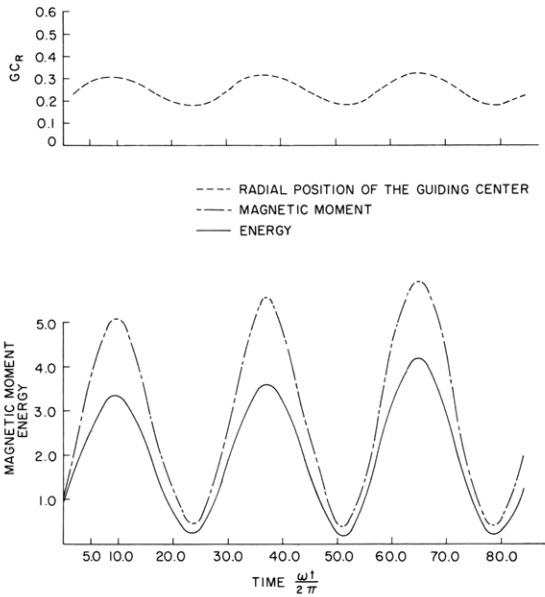

Fig. XV-22.

Energy, magnetic moment, and radial position of the guiding center as a function of time for a particle staying near to the midplane and starting in phase with the electric field.

followed the trajectory). The values of $\int v_{\parallel}ds$, along the magnetic field lines, taken between two consecutive reflection points, is approximately constant up to the 9th reflection point where it jumps suddenly and then stays constant; there is a sudden
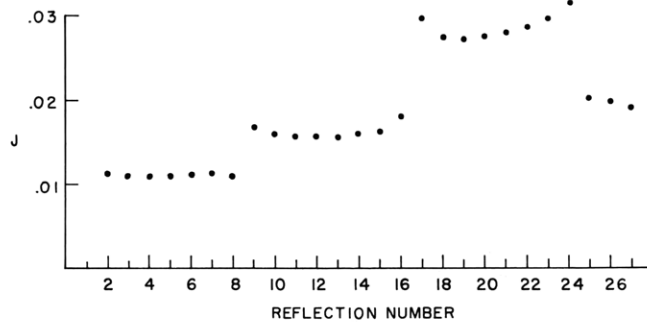
Fig. XV-23. Value of J ($\int v_{\parallel}$ ds between reflection points) at each reflection for the trajectory of Class II starting in phase with the electric field.

change again at the 16th reflection and at the 29th, all corresponding to the reflection during which the particle has a minimum of energy (see Fig. XV-23). The maximum displacement of the guiding center along the Z-axis is −.22134 at the 24th reflection point.

b. See Figs. XV-24 and XV-25. The initial velocity is out of phase with the electric field. The trajectory is similar to the corresponding one of Class I, but the

--- RADIAL POSITION OF THE GUIDING CENTER
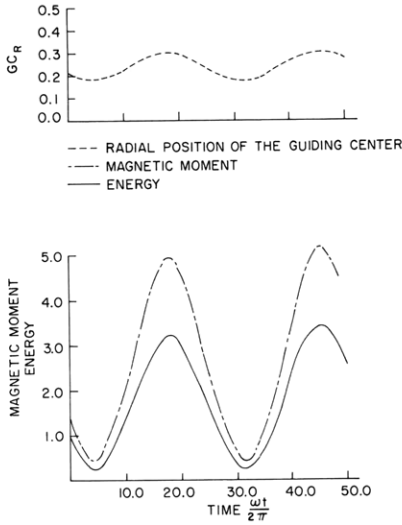-·-· MAGNETIC MOMENT
——— ENERGY

Fig. XV-24. Energy, magnetic moment, and radial position of the guiding center as a function of time for the trajectory of Class II starting out of phase with the electric field.

maxima of the energy and magnetic moment increase (during times that the trajectory has been followed). The values of $\int v_{\parallel} ds$ between reflection points remains approximately constant up to the 8th reflection point, then changes abruptly, and afterward
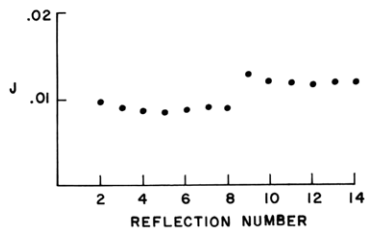

Fig. XV-25. Value of J ($\int v_{\parallel} ds$ between reflection points) at each reflection for the trajectory of Class II starting out of phase with the electric field.

remains constant. The trajectory was followed up to 14 reflections. During the 8th reflection the particle has a minimum of energy.

Trajectories of Class III

a. See Figs. XV-26 and XV-27. The particle starts in phase with the electric field. The particle moves along the field lines, sensing fields different from those at the midplane. Thus, the phase relation to the electric field is altered. After the 13th reflection, which occurs at 42.71 periods of the applied electric field, there is no resemblance of periodicity. After 22 reflections the particle has lost enough transverse energy to
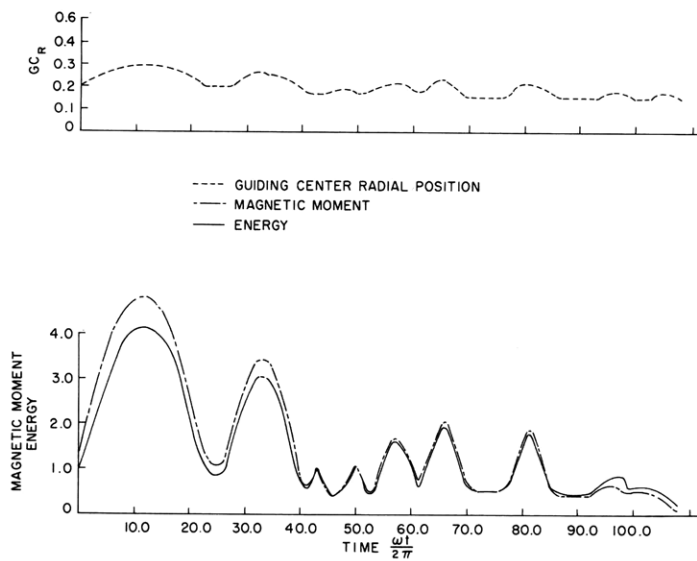
Fig. XV-26.   Energy, magnetic moment, and radial posi-
tion of the guiding center as a function of
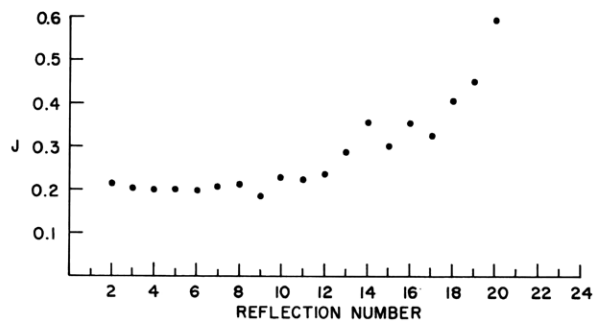time for the trajectory of Class III starting
in phase with the electric field.

Fig. XV-27.   Value of J ($\int v_{\parallel}$ ds between reflection
points) at each reflection for the tra-
jectory of Class III starting in phase
with the electric field.

escape from the mirrors. Initially the particle is not in the loss cone.

b. See Fig. XV-28. The initial velocity is out of phase with the electric field. The particle makes one reflection at z = 0.675 and goes out of the opposite end of the mirror.
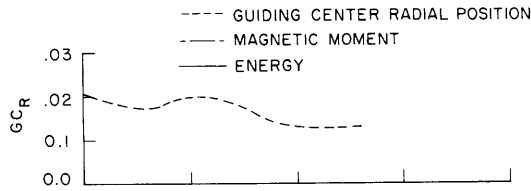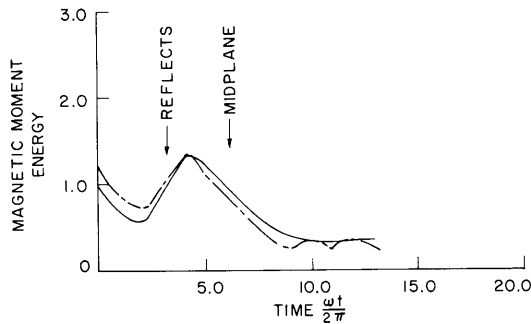

Fig. XV-28.

Energy, magnetic moment, and radial position of the guiding center as a function of time for the trajectory of Class III starting out of phase with the electric field.

The case of particles going deep into the mirrors is not realistic, however, because the electric field that is used has a large component along the magnetic field lines. In a plasma the electrons move freely along the magnetic field lines, tending to neutralize the component of the electric field parallel to the magnetic field lines.

Trajectories of Class II will be continued for longer times, in order to determine whether the maxima of the energy continue to grow. In order to consider more realistically the behavior of particles that go far into the mirrors, an electric field perpendicular to the magnetic field lines will be used. The magnitude of the electric field will be varied and the effect on the trajectories will be studied.

Appendix A. Initial Conditions for Trajectories

Class I

a. Starting in phase with the electric field

$$r_o = .12i_x + .09i_y$$

$$v_o = .8i_x + .6i_y$$

b. Starting out of phase with the electric field

$$r_o = .12i_x - .09i_y$$

$$v_o = .8i_x + .6i_y$$

Class II

a. Starting in phase

$$r_o = .12i_x + .09i_y$$

$$v_o = .79598992i_x + .59699263i_y + .1i_z$$

b. Starting out of phase

$$r_o = .12i_x - .09i_y$$

$$v_o = -.79598992i_x + .59699243i_y + .1i_z$$

Class III

a. Starting in phase

$$r_o = .125i_x + .085i_y$$

$$v_o = .75795162i_x + .51540709i_y$$

b. Starting out of phase

$$r_o = .125i_x - .085i_y$$

$$v_o = -.75795162i_x + .51540709i_y$$

Appendix B. Motion of a Particle in Crossed Uniform Fields $\doteq \vec{B}$ Constant, $\vec{E}$ Time-dependent, $\omega \neq \omega_B$ (see Fig. XV-29)
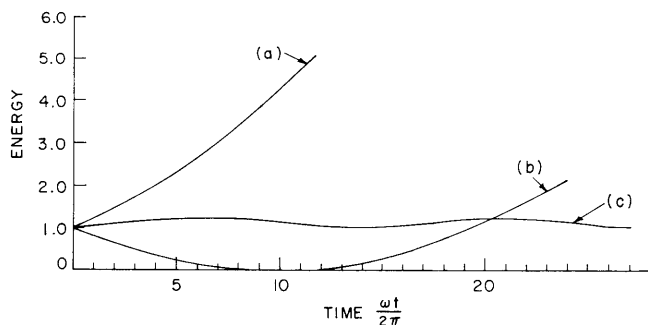

Fig. XV-29.

Energy as a function of time for the case of uniform static magnetic field and electric field. (a) In resonance $(\omega = \omega_B)$. Particle starting in phase with the electric field. (b) In resonance $(\omega = \omega_B)$. Particle starting out of phase with the electric field. (c) Off resonance $(\omega - \omega_B \approx 0.55)$.

The equation of motion is

$$\frac{d\vec{v}}{dt} + \frac{q}{mc} B_o \vec{i}_z \times \vec{v} = E_o \cos \omega t \vec{i}_x.$$

The solution is

$$v_x = v_x(0) \cos \omega_B t + v_y(0) \sin \omega_B t - \left[\frac{E_x(\omega-\omega_B)}{2(\omega+\omega_B)}\right] \sin \left[\frac{1}{2}(\omega+\omega_B)t\right] \cos \left[\frac{1}{2}(\omega-\omega_B)t\right]$$

$$+ \left[\frac{E_o(\omega+\omega_B)}{(\omega-\omega_B)}\right] \cos \frac{1}{2}(\omega+\omega_b)t \sin \frac{1}{2}(\omega-\omega_B)t.$$

The energy is given by

$$(K.E.) = (K.E.)_o + \frac{(qE_o)^2}{4m} \left[\frac{\sin^2 (\omega+\omega_b)t/2}{(\omega+\omega_b)^2} + \frac{\sin^2 (\omega-\omega_b)t/2}{(\omega-\omega_b)^2}\right].$$

For $\omega \sim \omega_b$, the last term dominates and the energy gain is approximately

$$W \approx \frac{(qE_o)^2}{4m} \frac{\sin^2 (\omega-\omega_b)t/2}{(\omega-\omega_b)^2}.$$

In our normalized units (see Quarterly Progress Report No. 85, pp. 186-192),

$$W = \frac{1}{2}\left(\frac{E_o}{RLR}\right)^2 \frac{\sin^2 (\Omega-\Omega_B)T/2}{(\Omega-\Omega_B)^2}.$$

O. Lopez, J. G. Siambis

XV. PLASMAS AND CONTROLLED NUCLEAR FUSION[*]

B. Applied Plasma Physics Related to Controlled Nuclear Fusion

Academic and Research Staff

Prof. D. J. Rose	Prof. L. M. Lidsky	Prof. S. Yip
Prof. T. H. Dupree	Prof. E. P. Gyftopoulos	Dr. K. Chung

Graduate Students

T. S. Brown	R. A. Hill	L. C. Pittenger
K. R-S. Chen	M. Hudis	A. Sugawara
D. G. Colombant	W. H. Manheimer	C. E. Wagner
R. W. Flynn	M. Murakami	A. Watanabe
	G. R. Odette	

1. NEUTRAL PARTICLE BEAMS WITH LARGE $\Delta E/E$

Introduction

Recent theoretical work by Rosenbluth and Post[1] indicates that the elimination of some velocity space instabilities and the minimization of others could be achieved by carefully controlling the trapped-particle energy distributions in high-temperature plasma machines. Because a modification of the injected particle beam appears to be one of the more convenient ways of modifying the trapped-particle distribution, we decided, late in 1965, to design and build a facility for production of neutral-particle beams with large $\Delta E/E$. This type of beam contrasts with present experimental practice, for which the injected beams have been monoenergetic, and microinstabilities have been observed.[2,3,4] Furthermore, because we are interested in the control of the trapped distribution for the purpose of studying instabilities, a large part of the work done on this problem has been the development of a computer model to predict the particle-energy distribution of the neutral beam.

Apparatus

The apparatus used in this experiment is shown in Fig. XV-30. It consists of a duoplasmatron ion source (upper left) that produces 20 keV hydrogen ions (H^+, H_2^+, and H_3^+) which are then mass-analyzed in a 90° bending magnet (lower left) so that only the H^+ component is focused into the horizontal beam line and experimental chamber (center of picture).

The energy-spreading device (Fig. XV-31 and center of Fig. XV-30) is a charge-exchange chamber operating at a variable pressure, using nitrogen as a target gas. Superimposed on the length of the charge-exchange region is a linear potential variation of 10 kV, so arranged that the incident beam has a minimum energy of 10 keV near the
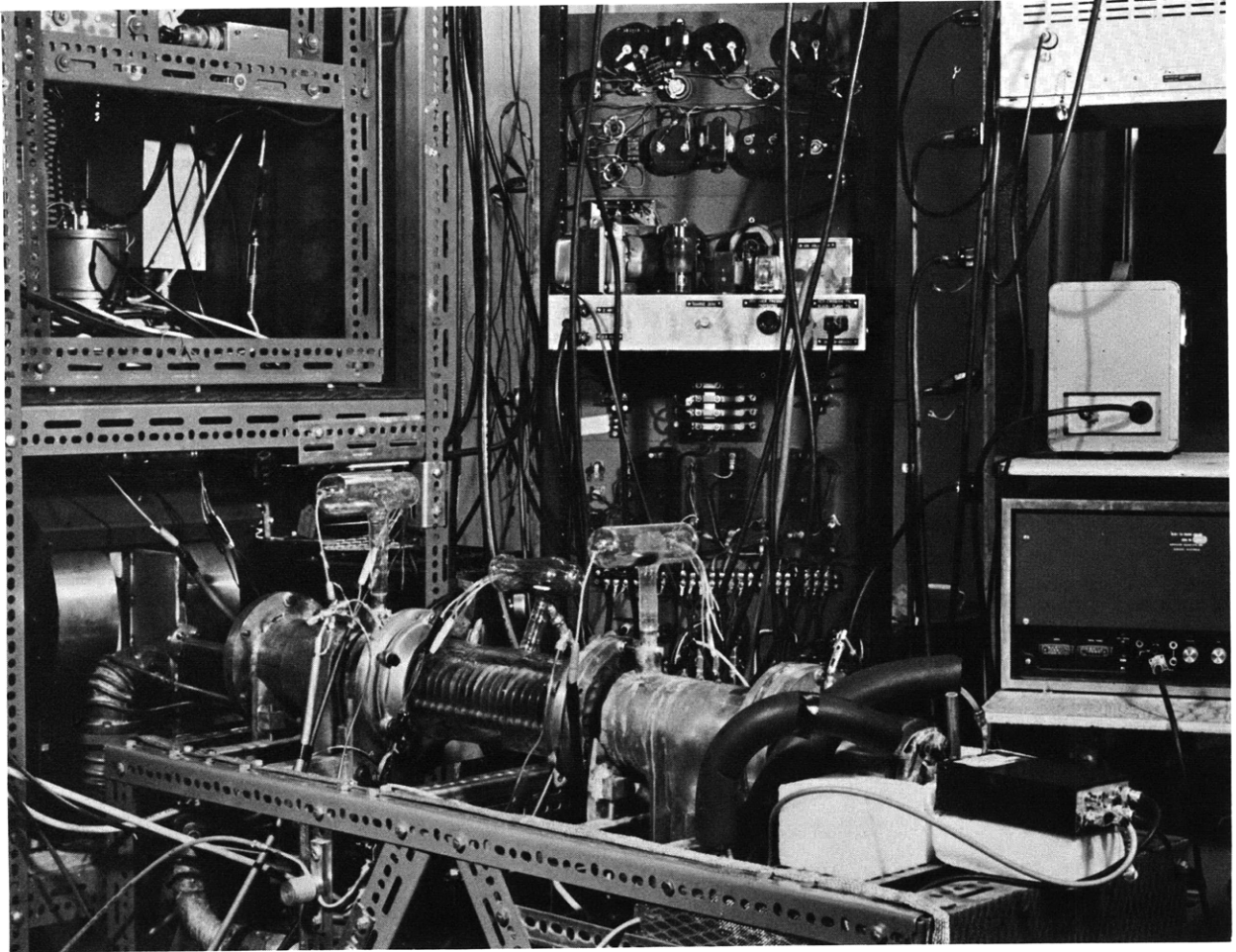
Fig. XV-30.   Apparatus used in the experiment.
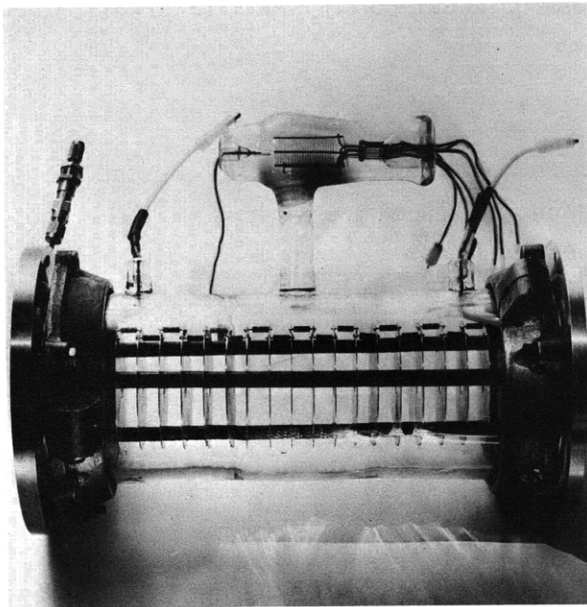
Fig. XV-31.   Energy-spreading device.

exit of the chamber. At the exit the ion component of the beam is deflected out of the beam line, and the neutral portion continues into the detection chamber for energy analysis.

Energy analysis of the neutral beam is done with a silicon barrier detector, whose response to an incident particle is amplified and fed into a 256-channel analyzer. By operating the detector at $-60°C$, a FWHM of 3.15 keV was obtained for the detector and associated electronics for an incident monoenergetic beam of 12-keV protons. Almost identical widths and linear response were obtained for monoenergetic particle beams in the energy range 9-25 keV, and these results (shown in Fig. XV-32) were used to calibrate the detector-multichannel analyzer response.
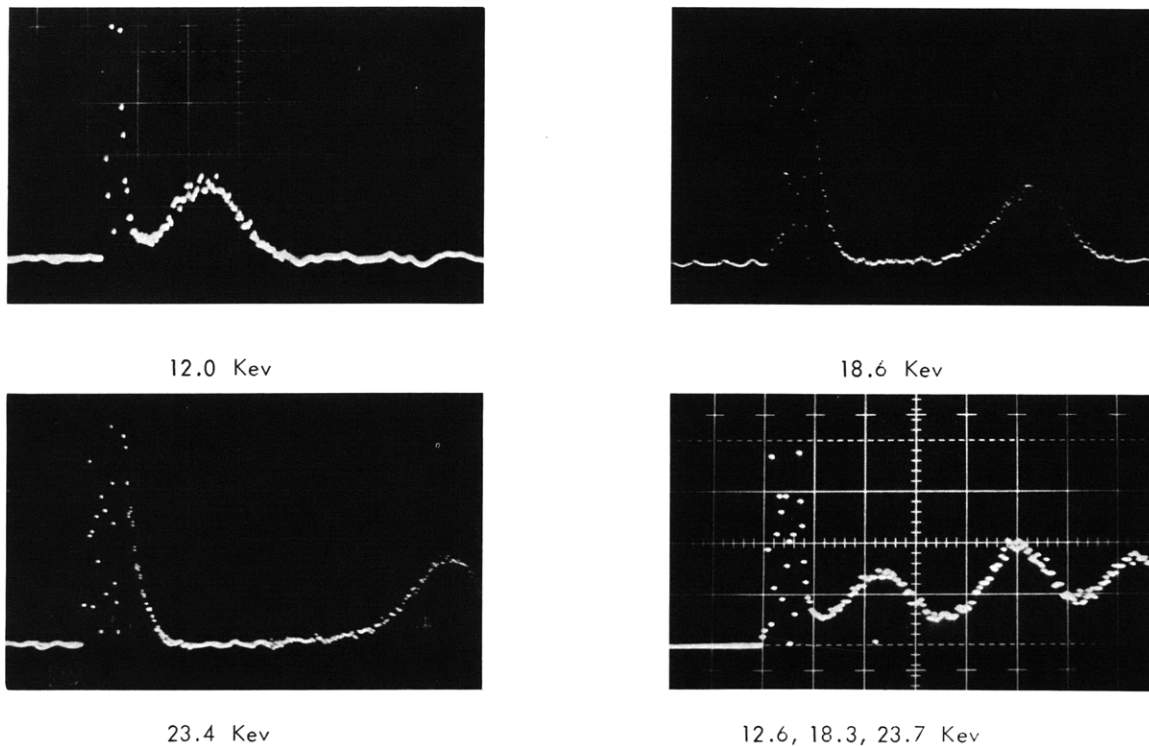

12.0 Kev

18.6 Kev

23.4 Kev

12.6, 18.3, 23.7 Kev

Fig. XV-32. Monoenergetic particle peaks.

A computer code was written to predict the behavior of the device. It solves the collision Boltzmann equation, using iterative procedures and linear approximations to the charge-transfer cross sections. The problem is complicated by the fact that the particles may change their charge state many times in their passage through the charge-exchange chamber, with the result that particle energy
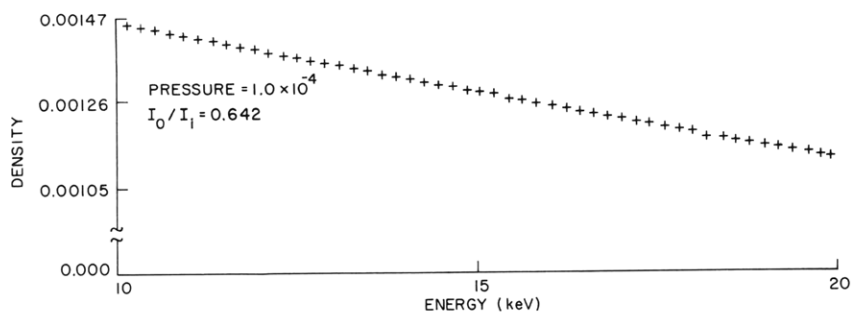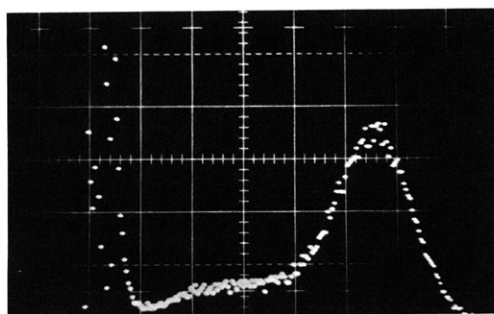
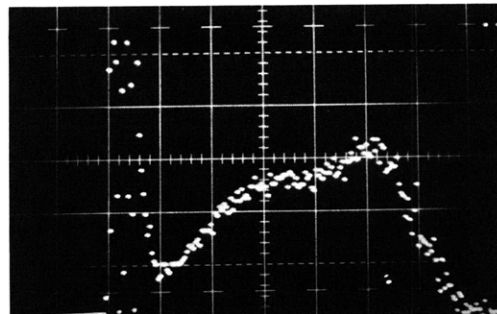Fig. XV-33.   Predicted particle energy distribution.

and position are not uniquely related. The results are plotted by using Calcomp plotter routines; a typical plot for $p = 1.0 \times 10^{-4}$ Torr is shown in Fig. XV-33.
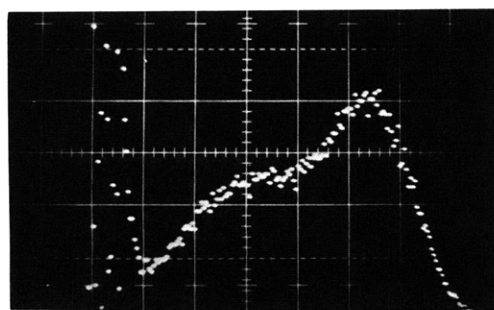
Results

Initial operation of the experiment produced results indicating that a significant portion of the beam was being neutralized in the region preceding the charge-exchange

Pressure $= 1 \times 10^{-4}$ torr
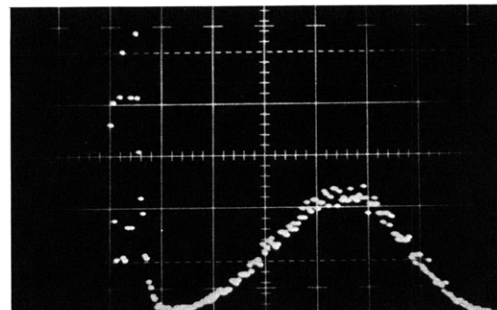

Pressure $= 1 \times 10^{-3}$ torr

Pressure $= 5 \times 10^{-4}$ torr

Pressure $= 5 \times 10^{-3}$ torr

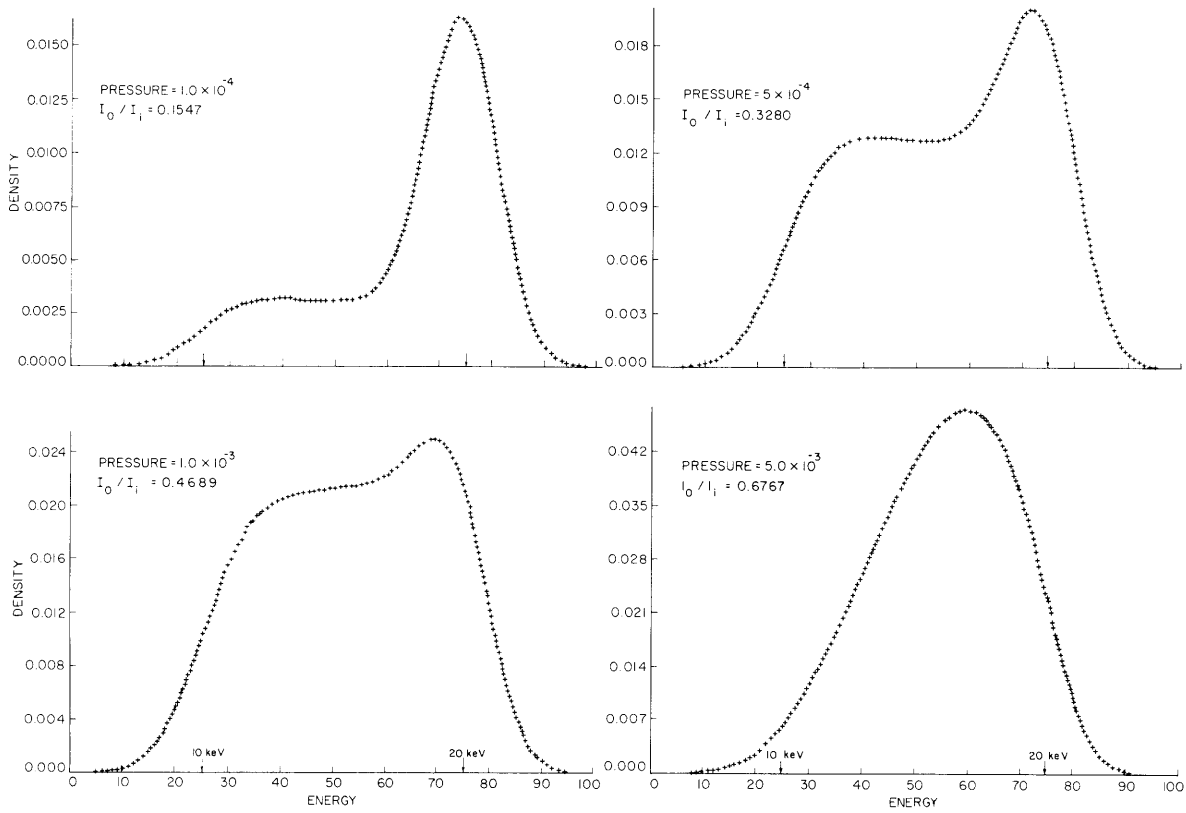Fig. XV-34.   Effect of pressure on particle energy distribution.

Fig. XV-35. Predicted particle energy distribution.

chamber. In order to easily compare this part of the experiment with the computer prediction, the results at all pressures were recalculated, under the assumption that 10% of the incident beam was neutral. This is the value inferred by measurements of the detector output at very low neutralization chamber pressures. The recalculation also included multiplying the computer results by a Green's function to take into account the finite detector response width. The results are shown in Fig. XV-35.

The results of the experiment are shown in Fig. XV-34 for 4 neutralization pressures. The peak on the extreme left of each picture is due to electronic noise, and the peak on the right of each of the low-pressure traces is due to the incident neutral beam. It is evident that the experimental and predicted results agree extremely well, both in ratio of height of the 20-keV neutral peak to height of the spectra, and in the general shape of the spectra. We conclude that it is not only possible to produce beams with large energy spreads, but also to predict their particle-energy distribution.

R. A. Hill, L. M. Lidsky

References

1. R. F. Post and M. N. Rosenbluth, "Electrostatic Instabilities in Finite Mirror-Confined Plasmas," Lawrence Radiation Laboratory Report UCRL-14388 (1965).

2. L. G. Kuo-Petravic et al., "R-F Stabilization of the Ion Cyclotron Instability in the Phoenix Experiment," a paper presented at the 8th Annual Meeting of the American Physical Society Division of Plasma Physics, Boston, Mass., November 2-5, 1966.

3. C. C. Damn et al., "Proton Containment in a Deep Magnetic Well," a paper presented at the 8th Annual Meeting of the American Physical Society Division of Plasma Physics, Boston, Mass., November 2-5, 1966.

4. C. C. Damn et al., Phys. Fluids 8, 1472 (1965).

XV. PLASMAS AND CONTROLLED NUCLEAR FUSION[*]

C. Plasma Magnetohydrodynamic Flows, Waves, and Instabilities

Academic and Research Staff

Prof. W. P. Allis   Prof. H. A. Haus

Graduate Students

C. A. McNary   K. R. Edwards

1. MAGNETOHYDRODYNAMIC WAVE PROPAGATION TRANSVERSE TO ELECTRIC CURRENT DENSITY

In an ordinary hydrodynamic fluid, stress is proportional to the temporal rate of change of strain. Since hydrodynamic stress is proportional to rate of strain and not to strain itself (as it is in an elastic solid), transverse mechanical waves do not occur in an ordinary hydrodynamic fluid. If, however, a magnetic field exists in a fluid with finite electric conductivity, then a magnetic Maxwell stress appears which is proportional to strain. This stress is significant if fluid motions occur within time scales shorter than the magnetic field relaxation time for the fluid. Thus, a magnetohydrodynamic fluid can support transverse waves — commonly called Alfvén waves. These waves are described by a combination of the quasi-static Ampere's law for a magnetic system, Faraday's law, Ohm's law (with $\omega_c \ll \nu$), and the conservation law for fluid momentum. For a highly conductive, homogeneous, isotropic fluid, the aforementioned combination yields a small-signal Alfvén wave equation for propagation along a uniform magnetic field

$$\frac{\partial^2 \psi}{\partial t^2} = a^2 \frac{\partial^2 \psi}{\partial z^2}; \qquad a^2 = \frac{B_o^2}{\rho_o \mu}. \tag{1}$$

But this equation does not hold for a collision-dominated, partially ionized plasma in which fluid motions occur with a time scale comparable with the magnetic field relaxation time, fluctuations in conductivity accompany wave motion, and equilibrium current density exists. This report is concerned with such a medium and the waves that it can support.

Physical assumptions incorporated in the mathematical model to be developed have been given in a previous report.[1] A description of the coordinate system embedded in the moving plasma and a glossary of symbol meanings are given in Table XV-1. The linearized equations of motion are Laplace-analyzed in space and time. The variables

---

Table XV-1. Coordinate system and glossary of symbols.

Coordinate System

$$\bar{i}_x = \bar{i}_y \times \bar{i}_z$$

$$\bar{i}_y \cdot \bar{J}_o = J_o$$

$$\bar{i}_z \cdot \bar{B}_o = B_o$$

$$\bar{k} \cdot \bar{J}_o = 0$$

Glossary

For a list of symbols, see Quarterly Progress Report No. 85, April 15, 1967, p. 202, and note the following changes:

Symbol	Definition
B_x, B_y, B_z	magnetic field components
E_x, E_y, E_z	electric field components
i_x, i_y, i_z	unit vectors
J_x, J_y, J_z	current density components
v_x, v_y, v_z	velocity components
θ	angle of propagation

are chosen to have the space-time dependence Re ζ exp($\omega t - k \cdot r$). In this report the wave number will be chosen as a real number, and the angular frequency will be sought analytically and numerically.

Conservation of Mass

$$\frac{\rho}{\rho_o} = \frac{k \sin \theta}{\omega} v_x + \frac{k \cos \theta}{\omega} v_z. \tag{2}$$

In the presence of an equilibrium current density, the Alfvén modes are not generally purely transverse.

Conservation of Momentum

$$\left(\frac{k}{\omega}\right) v_x = \left(\frac{k}{\omega}\right)^2 \sin\theta \gamma^{-1} s^2 \frac{p}{p_o} - i \frac{kJ_oB_o}{\rho_o\omega^2} \left(\frac{J_y}{J_o} + \frac{B_z}{B_o}\right) \tag{3a}$$

$$\left(\frac{k}{\omega}\right) v_y = i \frac{kJ_o B_o}{\rho_o \omega^2} \frac{J_x}{J_o} \tag{3b}$$

$$\left(\frac{k}{\omega}\right) v_z = \left(\frac{k}{\omega}\right)^2 \cos\theta \, \gamma^{-1} s^2 \frac{p}{p_o} + i \frac{kJ_o B_o}{\rho_o \omega^2} \frac{B_x}{B_o}. \tag{3c}$$

Except for linearly polarized Alfvén waves propagating along the equilibrium magnetic field with a y-directed small-signal magnetic field, the Alfvén mode velocity is not divergenceless for a finite equilibrium current density. The velocity divergence results from the interaction of the perturbed magnetic field with the equilibrium current density.

Ampere's Law
_____

$$\cos\theta \frac{B_y}{B_o} = -iI \frac{J_x}{J_o}; \qquad I = \frac{\mu J_o}{kB_o} \tag{4a}$$

$$\cos\theta \frac{B_x}{B_o} - \sin\theta \frac{B_z}{B_o} = iI \frac{J_y}{J_o} \tag{4b}$$

$$\sin\theta \frac{B_y}{B_o} = iI \frac{J_z}{J_o}. \tag{4c}$$

Faraday's Law
_____

$$\frac{\sigma_o}{J_o} \cos\theta E_y = -\frac{\sigma_o B_o (\omega/k)}{J_o} \frac{B_x}{B_o} \tag{5a}$$

$$\frac{\sigma_o}{J_o} \cos\theta E_x - \frac{\sigma_o}{J_o} \sin\theta E_z = \frac{\sigma_o B_o (\omega/k)}{J_o} \frac{B_y}{B_o} \tag{5b}$$

$$\frac{\sigma_o}{J_o} \sin\theta E_y = \frac{\sigma_o B_o (\omega/k)}{J_o} \frac{B_z}{B_o}. \tag{5c}$$

Equations 4a, 4c and 5a, 5c demonstrate the transverse nature of current and magnetic field, respectively.

Modified Ohm's Law
_____

$$\frac{J_x}{J_o} + \Omega_o \left[\frac{J_y}{J_o} + \frac{\Omega_z}{\Omega_o}\right] = \frac{\sigma_o}{J_o} E_x + \frac{\sigma_o B_o}{J_o} v_y + \Omega_o \frac{\sigma}{\sigma_o} \tag{6a}$$

$$\frac{J_y}{J_o} - \Omega_o \frac{J_x}{J_o} = \frac{\sigma_o}{J_o} E_y - \frac{\sigma_o B_o}{J_o} v_x + \frac{\sigma}{\sigma_o} \tag{6b}$$

$$\frac{J_z}{J_o} - \Omega_o \left(\frac{\Omega_x}{\Omega_o}\right) = \frac{\sigma_o}{J_o} E_z. \tag{6c}$$

In the previous report,[2] a brief physical interpretation of Eqs. 6a, 6b, and 6c can be found.

Thermodynamic Equation of State

$$\frac{p}{p_o} = \frac{\rho}{\rho_o} + \frac{T}{T_o}. \tag{7}$$

Conservation of Energy

$$\frac{T}{T_o} = \frac{R}{C_v} \left(\frac{k}{\omega}\right) [\sin\theta\, v_x + \cos\theta\, v_z] - i \left(\frac{k}{\omega}\right) a\gamma H \left[2\frac{J_y}{J_o} - \frac{\sigma}{\sigma_o}\right], \tag{8}$$

where

$$H = \frac{J_o^2/\sigma_o}{ka\rho_o C_p T_o}.$$

A brief physical interpretation of Eq. 8 and the constituent laws governing conductivity, collision frequency, and electron number density (herein referred to as Eqs. 9, 10, and 11, respectively) have been given previously.[3]

Hall Parameter

$$\frac{\Omega_x}{\Omega_o} = \frac{B_x}{B_o} \tag{12a}$$

$$\frac{\Omega_z}{\Omega_o} = \frac{B_z}{B_o} - \frac{\nu}{\nu_o}. \tag{12b}$$

The twenty linearized equations of motion and state listed above govern the 20 small-amplitude perturbations $(v_x, v_y, v_z, p, \rho, T, J_x, J_y, J_z, E_x, E_y, E_z, B_x, B_y, B_z, n_e, \nu, \sigma, \Omega_x, \Omega_y)$. In these equations the type of wave polarization has been left unspecified. Also, there is an additional equation representing Gauss' law for small-amplitude charge density, but it is coupled to the other 20 equations only through two of its three variables. It serves to define the perturbation charge density.

Gauss' Law

$$\frac{\sigma_o}{J_o} \cos\theta\, E_z + \frac{\sigma_o}{J_o} \sin\theta\, E_x = i \left(\frac{q_o}{J_o} \frac{\sigma_o/\epsilon}{k}\right) \frac{q}{q_o}. \tag{13}$$

The dispersion equation formed from the set of homogeneous equations (2)-(12) is of seventh degree in wave frequency. It is given in Table XV-2a. For small Hall parameter, the waves are approximately linearly polarized, while for large Hall parameter the waves are approximately circularly polarized. An understanding of the polarization can be obtained from Fig. XV-36. For small Hall parameter, the small-signal current density and electric field intensity are vectorially aligned so that the change in magnetic field takes the form of an amplitude variation, which results in linear polarization. For large Hall parameter, the current density and electric field intensity are spatially orthogonal so that the change in magnetic field takes the form of a vector reorientation, which results in circular polarization. For low current density and large magnetic Reynolds number and Hall parameter ($R_m \gg 1$, $\omega \ll \nu \ll \omega_c$), transverse propagation is characterized by 4 modes, two of which are heavily damped. The two remaining modes have the forms

$$\omega = \pm \Omega_o R_m^{-1} ka + i \frac{k^2}{2\mu_o \sigma_o} \tag{14a}$$

or

$$\omega = \pm \frac{\omega_c}{\mu \epsilon \omega_p^2} k^2 + i \frac{k^2}{2\mu \sigma_o}. \tag{14b}$$

These modes are commonly called helicon waves and are right circularly polarized. In this report, the discussion will be limited to the classical Alfvén wave regime for which the Hall parameter is small ($\omega_c \ll \nu$).

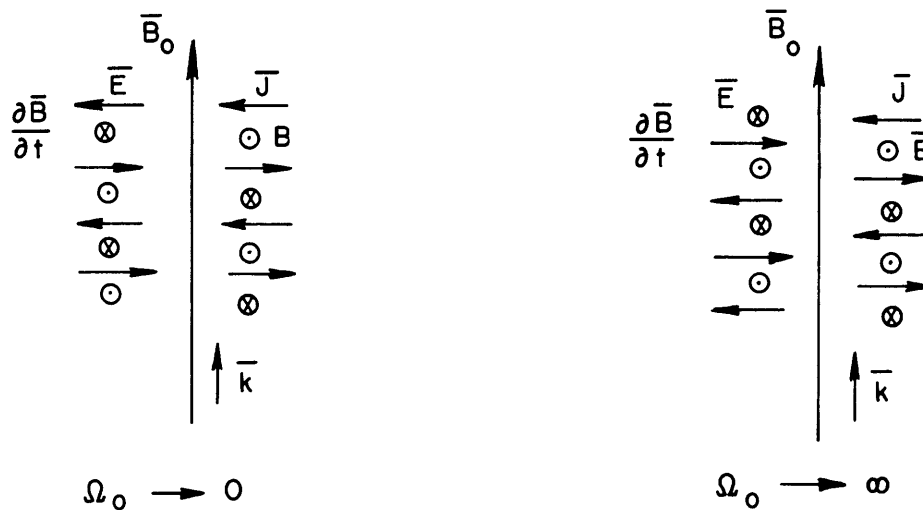If the terms involving Hall parameter in Table XV-2a are grouped together, the

Fig. XV-36. Description of Alfvén wave polarization.

Table XV-2a. Dispersion equation.

$$\omega_n^7 + \omega_n^6 \left\{ -i2R_m^{-1} - i\gamma\left(a + \frac{3}{4} - K_2\right)H \right\}$$

$$+ \omega_n^5 \left\{ -(1 + \cos^2\theta) - \left(\frac{\mathcal{R}}{1-\mathcal{R}}\right) - R_m^{-2}\left(1 + \Omega_0^2\cos^2\theta\right) + iI\sin\theta \right\}$$

$$+ \omega_n^4 \left\{ -2HI^{-1}\frac{\mathcal{R}}{1-\mathcal{R}}\sin\theta + IR_m^{-1}\sin\theta + iR_m^{-1}(1+\cos^2\theta) \right.$$

$$+ i2\left(\frac{\mathcal{R}}{1-\mathcal{R}}\right)R_m^{-1} + i\left(a + \frac{3}{4} - K_2\right)\gamma H\left[1 + \cos^2\theta + R_m^{-2}\left(1 + \Omega_0^2\cos^2\theta\right)\right]$$

$$+ i(K_1 - \beta)\left(1 + \frac{C_v}{R}\right)H\frac{\mathcal{R}}{1-\mathcal{R}} + \gamma\left(a + \frac{3}{4} - K_2\right)HI\sin\theta$$

$$\left. + \left[a + \frac{3}{4} - K_2 + \frac{C_v}{R}(\beta - K_1)\right]HI^{-1}\frac{\mathcal{R}}{1-\mathcal{R}}\sin\theta - i2\gamma HR_m^{-2}\left[\left(a + \frac{3}{4} - K_2\right) + \left(a + \frac{3}{4}\right)\Omega_0^2\cos^2\theta\right] \right\}$$

$$+ \omega_n^3 \left\{ +\cos^2\theta + 2\left(\frac{\mathcal{R}}{1-\mathcal{R}}\right)\cos^2\theta + \frac{\mathcal{R}}{(1-\mathcal{R})}\left(1 + \Omega_0^2\cos^2\theta\right)R_m^{-2} - iI\sin\theta\cos^2\theta \right.$$

$$+ i2HI^{-1}R_m^{-1}\frac{\mathcal{R}}{(1-\mathcal{R})}\sin\theta + \gamma\left(a + \frac{3}{4} - K_2\right)HR_m^{-1}\sin^2\theta$$

$$- i\left(a + \frac{3}{4} - K_2\right)HFR_m^{-1}\frac{\mathcal{R}}{(1-\mathcal{R})}\sin\theta - iHR_m^{-1}\frac{\mathcal{R}}{(1-\mathcal{R})}I^{-1}\sin\theta\left[\left(a + \frac{3}{4} - K_2 + \frac{C_v}{R}\beta - \frac{C_v}{R}K_1\right) + \left(a + \frac{3}{4} + \frac{C_v}{R}\beta\right)\Omega_0^2\cos^2\theta\right]$$

$$\left. - HR_m^{-1}\frac{\mathcal{R}}{(1-\mathcal{R})}\left[\left(a + \frac{3}{4} - K_2 + \frac{C_v}{R}\beta \cdot \frac{C_v}{R}K_1\right) + \left(a + \frac{3}{4} + \frac{C_v}{R}\beta\right)\Omega_0^2\cos^2\theta\right] \right\}$$

$$+ \omega_n^2 \left\{ 2\gamma^{-1}F^{-1}H\sin\theta\cos^2\theta - i2\frac{\mathcal{R}}{1-\mathcal{R}}R_m^{-1}\cos^2\theta - i\gamma\left(a + \frac{3}{4} - K_2\right)H\cos^2\theta \right.$$

$$- i\left(a + \frac{31}{4} - K_2 + K_1 - \beta\right)H\left(\frac{\mathcal{R}}{1-\mathcal{R}}\right)\left[2\cos^2\theta + R_m^{-2}\left(1 + \Omega_0^2\cos^2\theta\right)\right]$$

$$- \gamma\left(a + \frac{3}{4} - K_2\right)HI\sin\theta\cos^2\theta - \left[a + \frac{3}{4} - K_2 + \frac{C_v}{R}(\beta - K_1)\right]HI^{-1}\frac{\mathcal{R}}{1-\mathcal{R}}\sin\theta\cos^2\theta$$

$$+ i\left[a + \frac{3}{4} - K_2 + \frac{C_v}{R}(\beta - K_1)\right]H\frac{\mathcal{R}}{1-\mathcal{R}}\cos^2\theta + i2\left(a + \frac{3}{4} - K_2 + K_1 - \beta\right)H\frac{\mathcal{R}}{1-\mathcal{R}}R_m^{-2}$$

$$+ i2\left(a + \frac{3}{4} - \beta\right)H\left(\frac{\mathcal{R}}{1-\mathcal{R}}\right)R_m^{-2}\Omega_0^2\cos^2\theta - K_1\left(a + \frac{3}{4} - \frac{K_2}{K_1}\beta\right)HFR_m^{-2}\frac{\mathcal{R}}{(1-\mathcal{R})}\Omega_0^2\sin\theta\cos^2\theta$$

$$\left. + iK_1\left(a + \frac{3}{4} - \frac{K_2}{K_1}\beta\right)HIFR_m^{-2}\frac{\mathcal{R}}{(1-\mathcal{R})}\Omega_0^2\cos^2\theta \right\}$$

$$+ \omega_n^1 \left\{ -\left(\frac{\mathcal{R}}{1-\mathcal{R}}\right)\cos^4\theta \right\}$$

$$+ \omega_n^0 \left\{ +i\left(a + \frac{3}{4} - K_2 + K_1 - \beta\right)H\left(\frac{\mathcal{R}}{1-\mathcal{R}}\right)\cos^4\theta \right\} = 0,$$

where

$$K_1 = \frac{\nu_{ei_0}}{\nu_0}\left(1 - \frac{1}{2\ln\Lambda_0}\right)\beta + \frac{\nu_{en_0}}{\nu_0}$$

$$K_2 = \frac{\nu_{ei_0}}{\nu_0}\left(1 - \frac{1}{2\ln\Lambda_0}\right)\left(a + \frac{3}{4}\right) - \frac{3}{2}\frac{\nu_{ei_0}}{\nu_0}\left(1 - \frac{1}{\ln\Lambda_0}\right) - \frac{1}{2}\frac{\nu_{en_0}}{\nu_0}$$

$$a = \frac{\epsilon_i}{2k_BT_0}\left(1 - a_0^2\right) - \frac{3}{4}a_0^2 \qquad \beta = \frac{1}{2}\left(1 + a_0^2\right) \qquad \omega_n = \frac{\omega}{ka}.$$

Table XV-2b. Factored dispersion equation.

$$
\left\{\omega_n^2 - iR_m^{-1}\omega_n - \cos^2\theta\right\}\left[\omega_n^5 + \omega_n^4\left\{-iR_m^{-1} - i\gamma\left(a + \frac{3}{4} - K_2\right)H\right\}\right.
$$

$$
+\,\omega_n^3\left\{-1 - \frac{\mathcal{R}}{1-\mathcal{R}} + iI\sin\theta + \gamma\left(a + \frac{3}{4} - K_2\right)HR_m^{-1}\right\}
$$

$$
+\,\omega_n^2\left\{-2HI^{-1}\frac{\mathcal{R}}{1-\mathcal{R}}\sin\theta + i\frac{\mathcal{R}}{1-\mathcal{R}}R_m^{-1} + i(K_1-\beta)\left(1 + \frac{C_v}{R}\right)H\frac{\mathcal{R}}{1-\mathcal{R}}\right.
$$

$$
+\,i\gamma\left(a + \frac{3}{4} - K_2\right)H + \left(a + \frac{3}{4} - K_2\right)HF\frac{\mathcal{R}}{1-\mathcal{R}}\sin\theta
$$

$$
\left.+\left[a + \frac{3}{4} - K_2 + \frac{C_v}{R}(\beta - K_1)\right]HI^{-1}\frac{\mathcal{R}}{1-\mathcal{R}}\sin\theta\right\}
$$

$$
+\,\omega_n^1\left\{\frac{\mathcal{R}}{1-\mathcal{R}}\cos^2\theta - \left(a + \frac{3}{4} - K_2 + K_1 - \beta\right)HR_m^{-1}\frac{\mathcal{R}}{1-\mathcal{R}}\right\}
$$

$$
\left.+\,\omega_n^0\left\{-i\left(a + \frac{3}{4} - K_2 + K_1 - \beta\right)H\frac{\mathcal{R}}{1-\mathcal{R}}\cos^2\theta\right\}\right]
$$

$$
+\,\Omega_o^2\cos^2\theta\left[\omega_n^5\left\{-R_m^{-2}\right\} + \omega_n^4\left\{-i\gamma\left(a + \frac{3}{4} + K_2\right)HR_m^{-2}\right\}\right.
$$

$$
+\,\omega_n^3\left\{\frac{\mathcal{R}}{(1-\mathcal{R})}R_m^{-2} - i\left(a + \frac{3}{4} + \frac{C_v}{R}\beta\right)HR_m^{-1}\frac{\mathcal{R}}{(1-\mathcal{R})}I^{-1}\sin\theta\right.
$$

$$
\left.-\left(a + \frac{3}{4} + \frac{C_v}{R}\beta\right)HR_m^{-1}\frac{\mathcal{R}}{(1-\mathcal{R})}\right\}
$$

$$
+\,\omega_n^2\left\{+i\left(a + \frac{3}{4} - \beta - K_1 + K_2\right)H\frac{\mathcal{R}}{(1-\mathcal{R})}R_m^{-2} + iK_1\left(a + \frac{3}{4} - \frac{K_2}{K_1}\beta\right)HIFR_m^{-2}\frac{\mathcal{R}}{(1-\mathcal{R})}\right.
$$

$$
\left.\left.-K_1\left(a + \frac{3}{4} - \frac{K_2}{K_1}\beta\right)HFR_m^{-2}\frac{\mathcal{R}}{(1-\mathcal{R})}\sin\theta\right\}\right] = 0
$$

remaining terms can be factored into a product of a second- and fifth-degree dispersion polynomial, as given in Table XV-2b. From this factoring it is evident that 2 modes of propagation remain uncoupled from the other 5 modes for small Hall parameter. These two modes represent linearly polarized Alfvén waves with small signal current density transverse to the equilibrium current density. For these modes there is no change in Joule heating intensity arising from small-signal current. Also, the small-signal magnetic field is oriented along the equilibrium current so that it does not interact with equilibrium current flow to produce a small-signal compressional force. Consequently, this pair of modes is uncoupled from the parameter variations mode and the acoustic modes. It is also spatially orthogonal to a separate pair of linearly polarized Alfvén modes with small-signal current density along the equilibrium current density.

Analytic solutions of the dispersion equation are stated for three limiting cases which are motivated by physical insight. First, analytic solutions for characteristic frequencies are obtained in the limit of low current density. This limit is suggested by the fact that parameter variations have a negligible effect for low current density and are uncoupled from the acoustic and Alfvén roots. Second, analytic solutions are obtained in the limit of large Euler number ($E_{ul} = p_o/\rho_o a^2$), and finally in the limit of

small Euler number. These last two limits are motivated by a desire to uncouple the acoustic modes in such a manner that the remaining modes can be examined.

Low Current Density Limit

This limit considers solutions to first order in current such that $\dfrac{J_o B_o}{p_o k}$, $\dfrac{\mu J_o}{k B_o} \sim \mathcal{O}(\epsilon)$, $\epsilon \ll 1$. Furthermore, solution is facilitated by choosing a large magnetic Reynolds number, $R_m^{-1} = \dfrac{k}{\mu \sigma_o a} \sim \mathcal{O}(\epsilon)$, with the Alfvén and acoustic speeds of the same order of magnitude. The result is that for $\theta = 0$ and to first order in ϵ,

$$\omega_1 = ks \qquad \text{(positive acoustic mode)} \tag{15a}$$

$$\omega_2 = -ks \qquad \text{(negative acoustic mode)} \tag{15b}$$

$$\omega_3 = 0 \qquad \text{(parameter variations mode)} \tag{15c}$$

$$\omega_4 = \left[1 - i \left(\frac{R_m^{-1}}{2} \right)^2 \right]^{1/2} ka + i \frac{k^2}{2\mu\sigma_o} \qquad \text{(positive Alfvén mode, } B \perp J_o) \tag{15d}$$

$$\omega_5 = -\left[1 - i \left(\frac{R_m^{-1}}{2} \right)^2 \right]^{1/2} ka + i \frac{k^2}{2\mu\sigma_o} \qquad \text{(negative Alfvén mode, } B \perp J_o) \tag{15e}$$

$$\omega_6 = \left[1 - i \left(\frac{R_m^{-1}}{2} \right)^2 \right]^{1/2} ka + i \frac{k^2}{2\mu\sigma_o} \qquad \text{(positive Alfvén mode, } B \parallel J_o) \tag{15f}$$

$$\omega_7 = -\left[1 - i \left(\frac{R_m^{-1}}{2} \right)^2 \right]^{1/2} ka + i \frac{k^2}{2\mu\sigma_o} \qquad \text{(negative Alfvén mode, } B \parallel J_o). \tag{15g}$$

This limit serves to identify all 7 modes and to demonstrate that in the absence of large equilibrium current density, and consequently in the absence of parameter variations effects, all characteristic modes are stable.

Large Euler Number Limit

This limit corresponds to mode oscillation on a time scale sufficiently long for fluid inertia to be negligible. Pressure gradients in the fluid counterbalance small-signal changes in the Lorentz force density. In addition to $E_{ul}^{-1} \sim \mathcal{O}(\epsilon)$, consider αH, $\zeta_2/(\gamma-1)\zeta_1 \sim \mathcal{O}(\epsilon)$, where

$$\frac{\sigma}{\sigma_o} = \zeta_1 \frac{T}{T_o} + \zeta_2 \frac{\rho}{\rho_o}.$$

The last assumption simplifies the presentation of the solution by considering conductivity variations to be only a function of small-signal temperature changes. For $\theta = 0$, to $\mathcal{O}(\epsilon)$ the dispersion equation can be factored into three parts.

$$(\omega^2 - k^2 s^2) = 0 \qquad\qquad (\omega_1, \omega_2) \qquad\qquad\qquad (16a)$$

$$(\omega - i a H k a)\left(\omega^2 - i \frac{k^2}{\mu \sigma_o} \omega - k^2 a^2\right) = -i a H k a \omega^2 - 2 a H \frac{k^2}{\mu \sigma_o} k a \omega \qquad (\omega_3, \omega_4, \omega_5) \qquad (16b)$$

$$\left(\omega^2 - i \frac{k^2}{\mu \sigma_o} \omega - k^2 a^2\right) = 0 \qquad (\omega_6, \omega_7) \qquad\qquad\qquad (16c)$$

From Eqs. 16a and 16c it is evident that the solutions for ω_1, ω_2, ω_6, and ω_7 are the same as those for the low current density limit. The terms on the right-hand side of Eq. 16b serve to couple ω_3 with ω_4 and ω_5. The first term on the right represents the effects of the interaction of small-signal changes in the Lorentz force density, because of variations in magnetic field intensity. The second term represents the first-order effect of small-signal changes in the Joule heating intensity resulting from variations in current density. To $\mathcal{O}(\epsilon)$,

$$\omega_3 = i a H k a \qquad\qquad\qquad\qquad (17a)$$

$$\omega_4 = \left[1 - \frac{1}{2} a H R_m^{-1}\right] k a + i \frac{ka}{2}\left[R_m^{-1} - a H\right] \qquad (17b)$$

$$\omega_5 = -\left[1 - \frac{1}{2} a H R_m^{-1}\right] k a + i \frac{ka}{2}\left[R_m^{-1} - a H\right]. \qquad (17c)$$

The first pair of Alfvén modes exhibits an instability whenever

$$a H R_m > 1. \qquad\qquad\qquad\qquad (18)$$

In Fig. XV-37, the dynamics of instability are shown. As the Alfvén modes (ω_4, ω_5) propagate, changes in the Lorentz force density associated with the small-signal magnetic field strength produce compressions and rarefactions in the fluid. These fluid density (and temperature) variations occur in phase with wave propagation when the fluid has negligible inertia. The changes in fluid temperature are accompanied by conductivity fluctuations that cause small-signal current changes so as to reinforce the ordinary small-signal current. The strength of this reinforcement (which occurs during each wave cycle) is proportional to aH. Losses resulting from finite conductivity are represented by the appearance of a magnetic Reynolds number, R_m, in Eq. 18. The

first-order shift in the real parts of ω_4 and ω_5 is due to small-signal Joule heating inten-
sity variations. In summary, a physical mechanism for the instability of Alfvén waves
has been exposed. Its existence depends upon the presence of a finite current density
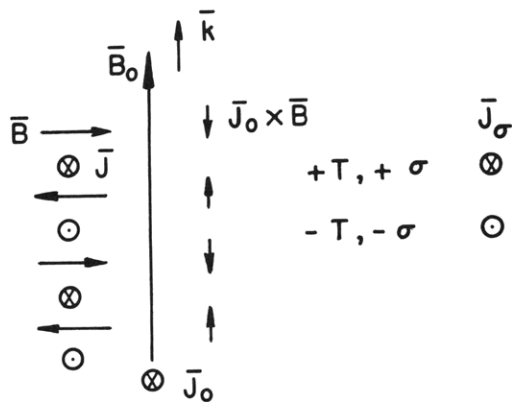and upon conductivity fluctuations.

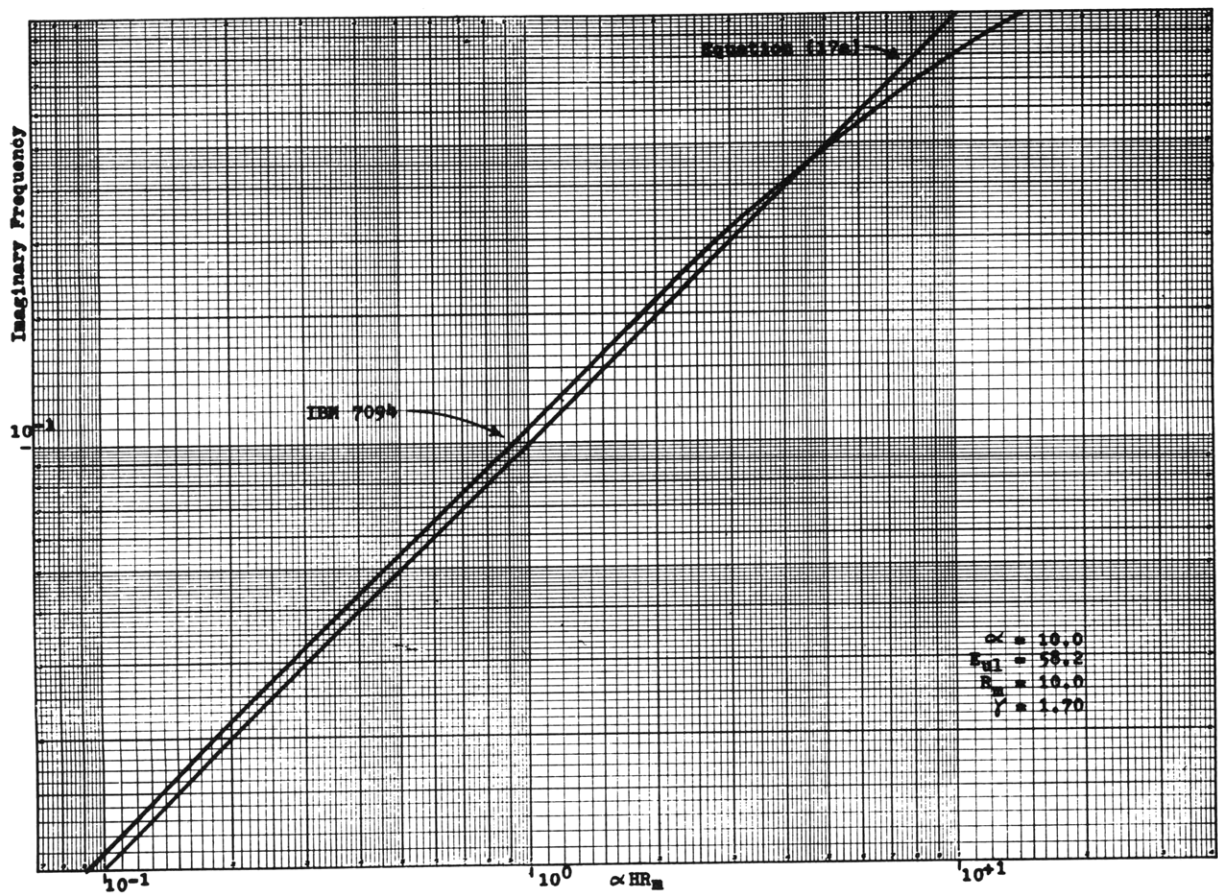Fig. XV-37. Dynamics of instability in Alfvén
modes 4 and 5.

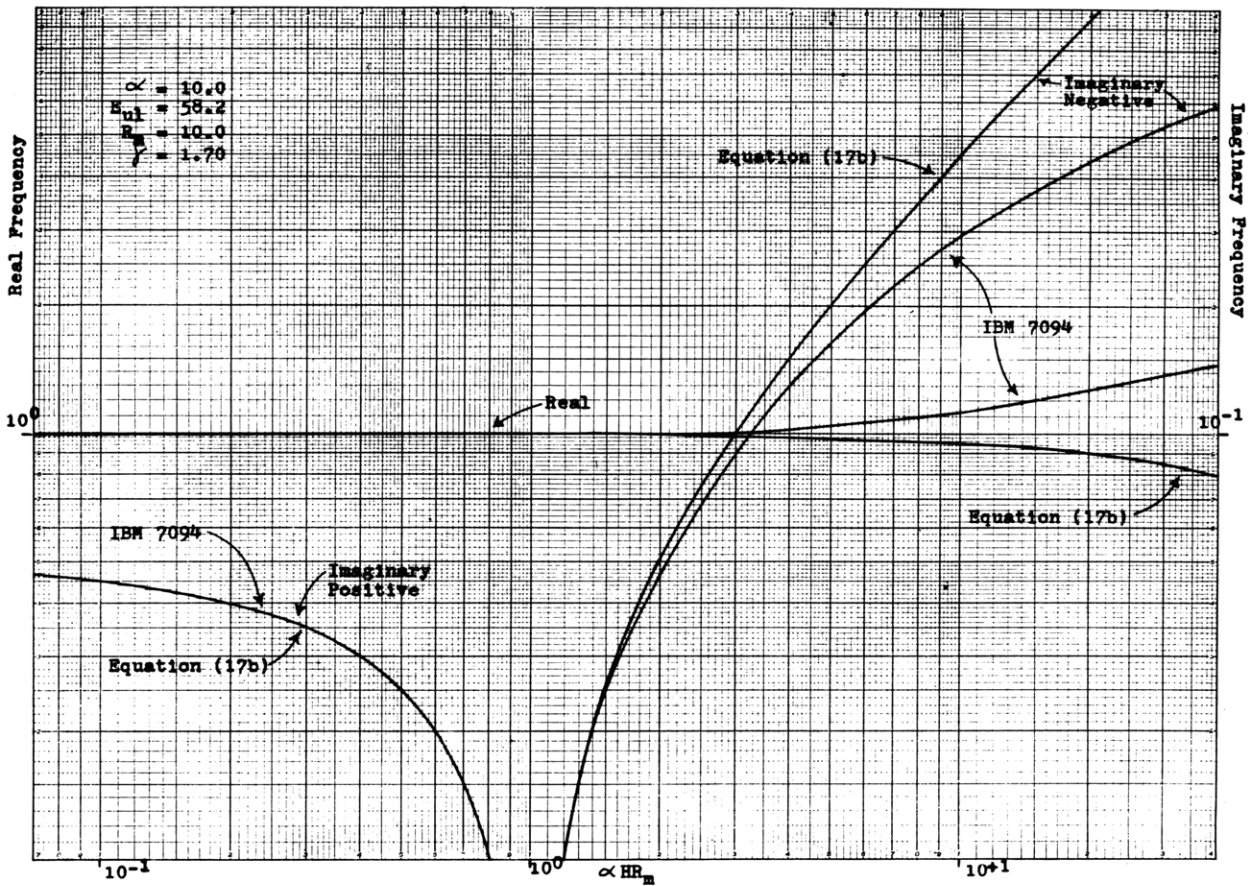Fig. XV-38. Comparison of Eq. 17a with numerical solutions of the dispersion equation.

Fig. XV-39.   Comparison of Eq. 17b with numerical solutions of the dispersion equation. Identical curves can be drawn for Eq. 17c, but with negative real parts for the analytic and numerical solutions.

Small Euler Number Limit

This limit corresponds to mode oscillation on a time scale that is short enough for fluid motion to be inertia-dominated. The fluid inertial force density counterbalances small-signal changes in the Lorentz force density. In addition to $E_{ul} \sim \mathcal{O}(\epsilon)$, again consider aH, $\zeta_2/(\gamma-1)\zeta_1 \sim \mathcal{O}(\epsilon)$. For $\theta = 0$, to $\mathcal{O}(\epsilon)$ the dispersion equation again factors into three parts as in Eqs. 16a, 16b, and 16c, but with Eq. 16b replaced by Eq. 19.

$$(\omega - i\gamma aHka)\left(\omega^2 - i\frac{k^2}{\mu\sigma_o}\omega - k^2 a^2\right) = -2a\gamma H\frac{k^2}{\mu\sigma_o}ka\omega. \tag{19}$$

The first term on the right of Eq. 16b does not appear in Eq. 19, since it represents changes in pressure, density, and temperature produced by the small-signal Lorentz force density. These changes cannot occur if the fluid is inertia-dominated, and consequently the Alfvén modes will remain stable.
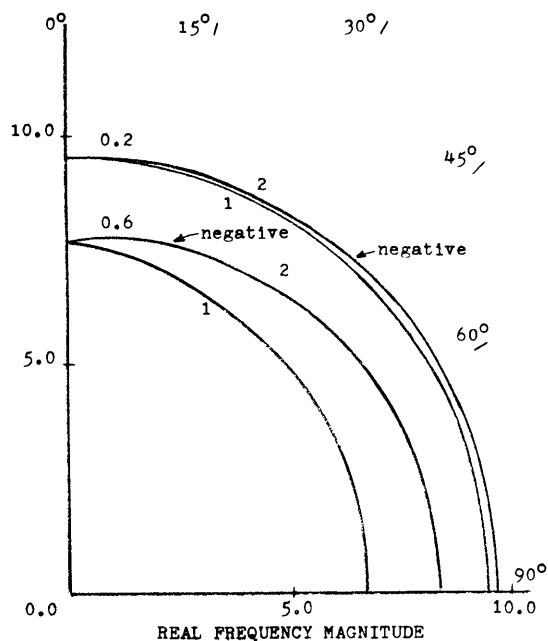
Fig. XV-40.

Polar plot of the real frequency of acoustic modes 1 and 2 with respect to angle of propagation for H = 0. 2 and 0. 6.
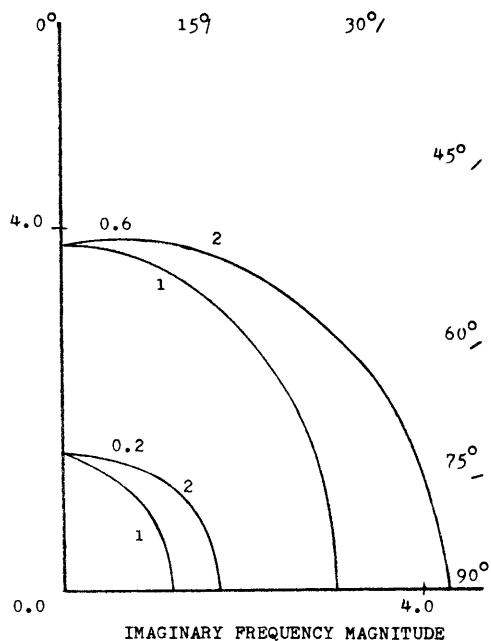
Fig. XV-41.

Polar plot of the imaginary frequency of acoustic modes 1 and 2 with respect to angle of propagation for H = 0.2 and 0.6.
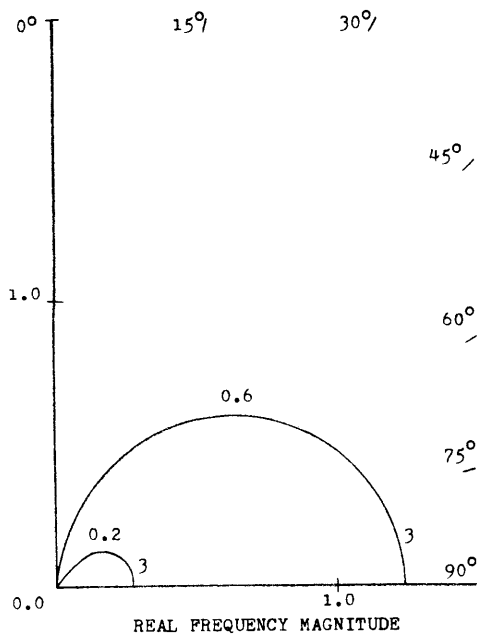
Fig. XV-42.

Polar plot of the real frequency of parameter variations mode 3 with respect to angle of propagation for H = 0. 2 and 0. 6.
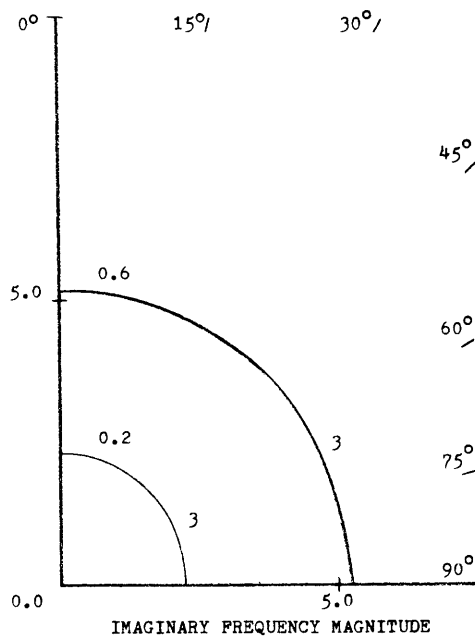
Fig. XV-43.

Polar plot of the imaginary frequency of parameter variations mode 3 with respect to angle of propagation for H = 0.2 and 0.6.
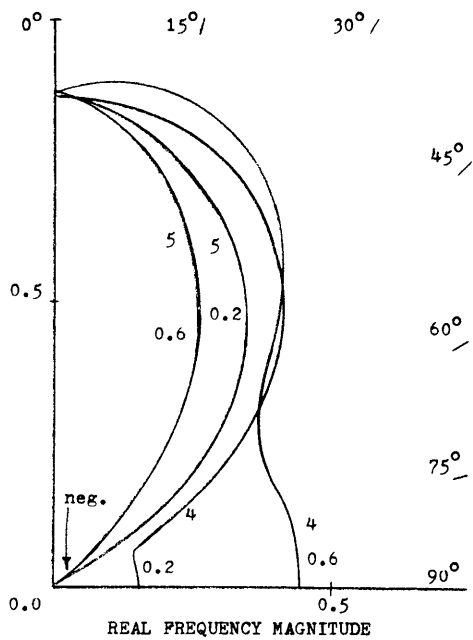
Fig. XV-44.

Polar plot of the real frequency of coupled Alfvén modes 4 and 5 with respect to angle of propagation for H = 0.2 and 0.6. Compare with uncoupled Alfvén modes 6 and 7 in Fig. XV-46.
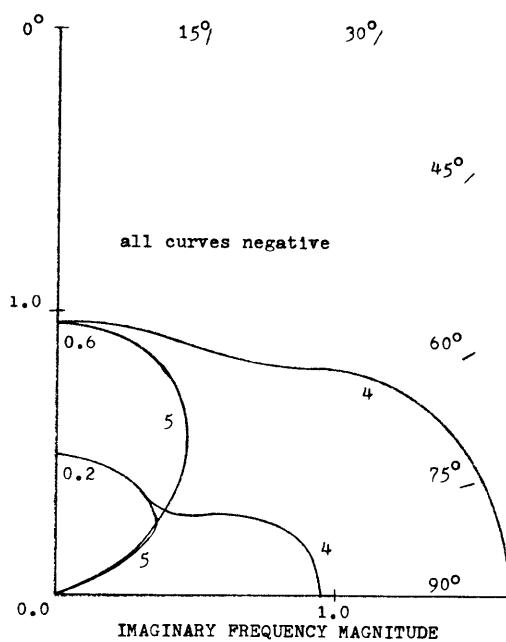

Fig. XV-45.

Polar plot of the imaginary frequency of coupled Alfvén modes 4 and 5 with respect to angle of propagation for H = 0.2 and 0.6. Compare with uncoupled Alfvén modes 6 and 7 in Fig. XV-47.
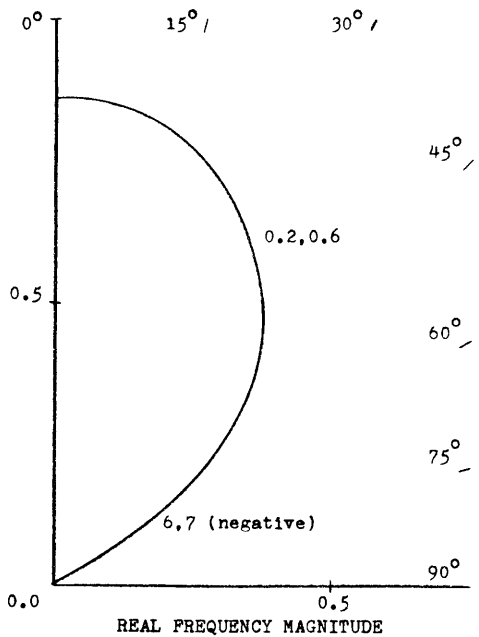

Fig. XV-46.

Polar plot of the real frequency of uncoupled Alfvén modes 6 and 7 with respect to angle of propagation for H = 0.2 and 0.6.
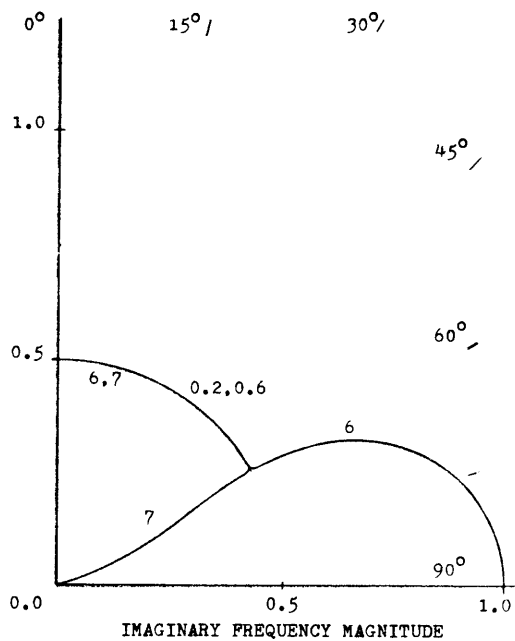

Fig. XV-47.

Polar plot of the imaginary frequency of uncoupled Alfvén modes 6 and 7 with respect to angle of propagation for H = 0.2 and 0.6.

Numerical Solutions

The characteristic roots of the complete one-fluid dispersion equation derived from homogeneous equations (2)-(12) were found numerically by using the M.I.T. Computation Center's IBM 7094 computer. Solutions were sought in order to ascertain the validity of analytic descriptions presented in this report. Some critical comparisons of analytic and numerical solutions are plotted in Figs. XV-38 and XV-39. In these figures, analytic solutions are valid for $aHR_m = \mathscr{O}(1.0)$ or less. Solutions are also given in Figs. XV-40 through XV-47 in the form of Friedrichs-like diagrams for real wave number, with the characteristic frequencies normalized to the Alfvén wave frequency. Curves are presented for $a = 10.0$, $E_{ul} = 58.2$, $R_m = 1.0$, $\gamma = 1.7$, and H = 0.2 and 0.6. The characteristic modes are identified by means of integer labels. For example, in Fig. XV-40 the real frequency is plotted for modes 1 and 2, with $aHR_m = 2.0$ and 6.0.

For propagation along the magnetic field ($\theta = 0$) there is no preferential direction. Consequently, modes of propagation occur in symmetrical pairs: the curves for modes 1 and 2, 4 and 5, 6 and 7 are coincident for $\theta = 0$. Similarly, the real frequency of mode 3 goes to zero as the propagation angle approaches zero. As previously discussed, a preferential direction exists for $\theta \neq 0$, and therefore the aforementioned symmetry does not occur except for propagation along the magnetic field. As H increases from 0.2 to 0.6, the lack of symmetry becomes more apparent. Alfvén modes 4 and 5 (Figs. XV-44 and XV-45), which are coupled to parameter variations effects, should be compared with Alfvén modes 6 and 7 (Figs. XV-46 and XV-47), which are uncoupled. For $\theta = 90°$, Alfvén mode 4 has a nonzero real frequency (see discussion of magnetic diffusion mode in the previous report[2]). The parameter variations mode 3 has an increased real phase velocity when H is increased.

K. R. Edwards

References

1. H. A. Haus, J. E. McCune, and K. R. Edwards, "Magnetohydrodynamic Wave Propagation Transverse to Magnetic Fields," Quarterly Progress Report No. 85, Research Laboratory of Electronics, M.I.T., April 15, 1967, p. 202.

2. Ibid., pp. 201-216.

3. Ibid., pp. 204-205.